CR-134003

STANFORD BISTATIC RADAR EXPERIMENT (S-170) ON APOLLOS 14, 15, AND 16

by

H. T. Howard

G. L. Tyler

July 1973

Final Report

Prepared under

National Aeronautics Space Administration

Contract NAS 9-10579

RADIOSCIENCE LABORATORY

STANFORD ELECTRONICS LABORATORIES

STANFORD UNIVERSITY • STANFORD, CALIFORNIA

STANFORD BISTATIC RADAR EXPERIMENT (S-170) ON APOLLOS 14, 15, and 16

by

H. T. Howard

G. L. Tyler

July 1973

Final Report

Prepared under

National Aeronautics Space Administration

Contract NAS 9-10579

CONTENTS

I. Introduction

This is the final contract and scientific mission analysis report required under contract number NAS 9-10579 between the NASA and Leland Stanford Junior University. This work was suggested in a proposal that S-band (13 cm) radio frequency transmissions from the lunar orbiting Command Service Module be used to obtain bistatic radar echoes from the lunar surface. The reception of these echoes was to be carried out on the earth. The proposal was accepted and a contract initiated with an authorization to incur cost dated January 29, 1970. The period of performance was from that date through June 30, 1973.

Subsequently, it was realized that VHF (116 cm) radio frequency transmissions were also available and could be used for bistatic radar purposes. Due to the straight forward nature of the experiment and the fact that no special on-board equipment was required, it was agreed that the bistatic experiments would be carried out as early as possible in the mission set. The initial experiment schedule included VHF observations on Apollo 13, and both S-band and VHF observations simultaneously on Apollos 14 and 15. These observations were later expanded to include the simultaneous dual wavelength experiment on Apollo 16 as well. No observations were obtained from Apollo 13 due to the unfortunate circumstances associated with that mission. Simultaneous S-band and VHF observations were obtained on each of the three subsequent missions of Apollos 14, 15 and 16.

II. Experiment Purpose

The purpose of S-170 was to:

1. Determine the principal electromagnetic parameters of the lunar crust;

2. Determine the electromagnetic properties of lunar regolith and subsurface structure to depths of at least several tens of meters;

3. Determine the frequency dependence, if any, of the principal crustal electromagnetic parameters;

4. Determine the presence of vertical surface structure and spatial distribution of horizontal surface structure within the range given above with emphasis placed on the depth of the regolith.

5. Map the statistical properties of surface roughness on the scales of the wavelength employed.

In general, we have attempted to develop quantitative measures of lunar surface properties that can be used to characterize and define lunar surface structure. These results have then been applied to the larger problem of lunar evolution and state through collaboration with colleagues in the geological and geophysical sciences.

III. Publications

To date this experiment has resulted in the following publications:

Tyler, G. L. with Thompson, T. W. et al., "Remote Sensing of Mare Serenitatis," to appear in Apollo 17 Preliminary Science Report, NASA.

Tyler, G. L. with Moore, H. J. "Comparison Between Photogrammetric and Bistatic-Radar Slope-Frequency Distributions," to appear in Apollo 17 Preliminary Science Report, NASA.

Tyler, G. L. and Howard, H. T., "Dual Frequency Bistatic Radar Investigations of the Moon with Apollos 14 and 15," J. Geophys. Res., to appear August, 1973.

Parker, M. N. and Tyler, G. L., "Bistatic Radar Estimation of Surface Slope Probability Distributions with Applications to the Moon," Radio Science, 8, pp. 177-184, March, 1973.

Howard, H. T. and Tyler, G. L., "Bistatic Radar Investigation," Apollo 16 Preliminary Science Report, NASA Publication SP-315, pp. 25-1 - 25-13, 1973.

Howard, H. T. and Tyler, G. L., "Bistatic Radar Investigation," Apollo 15 Preliminary Science Report, NASA Publication SP-289, pp. 23-1 - 23-10, 1972.

Howard, H. T. and Tyler, G. L., "Bistatic Radar Studies of the Lunar Surface," Apollo 14 Preliminary Science Report, NASA Publication SP-272, pp. 247-266, 1971.

IV. Experiment Discussion and Results

Observational data records, reduced data, and a detailed report of the data reduction process from this experiment have been submitted to the National Space Science Data Center. A copy of the NSSDC report (Stanford-Apollo Bistatic-Radar Experiment (S-170): National Space Science Data Center Data Description) is bound with this report. It contains the principal technical details of the experiment.

Additional observations were carried out using the 116 cm wavelength alone. Approximately three times more data were obtained in this mode than in the dual wavelength case. The single wavelength observations represent an experiment of opportunity in that by agreement with JSC the experimenters exercised no control over the lunar ground track, the time of observation, or the spacecraft antenna directivity with respect to the experimental geometry. Consequently, these observations are somewhat less useful than those obtained at the dual wavelength in terms of direct in inference of surface properties. However, since data were obtained on sequential orbits, a two dimensional scanning action across the lunar surface was obtained. Thus, these data are quite valuable for mapping two dimensional variations in lunar scattering

properties. Due to the heavy emphasis on the dual wavelength observations, these data have received little attention thus far.

This experiment grew from earlier work with Lunar Orbiters I, III, (Tyler et al. 1967) and Lunar Explorer 35 (Tyler 1968). The Lunar Orbiter observations provided the first bistatic-radar echoes from the moon, demonstrated the feasibility of such experiments, and indicated that oblique incidence forward scattering from the lunar surface was dominated by quasi-specular scattering mechanisms. The first systematic, scientific investigation of an extraterrestrial body using the bistatic radar technique was carried out with Explorer 35 spacecraft. Only a single wavelength (2.2 meters) was available for these observations. The results of these experiments have been reported elsewhere (e.g., v. Tyler 1968; Tyler and Simpson 1970; Tyler, Simpson and Moore 1971).

The Apollo observations continued this work. Although the data set obtained is more limited with respect to coverage than that from Explorer 35, the experimental controls were much more stringent and the experimental signal-to-noise ratio was approximately an order of magnitude higher. The simultaneous, dual-wavelength nature of this experiment is unique. First order analysis and interpretation of the dual-wavelength data have been completed. From the conclusions of Tyler and Howard , (1973):

> "The oblique geometry scattering properties of the lunar surface are wavelength dependent in the decimeter to meter wavelength range. At a fixed wavelength, the scattering law is highly dependent on local topography. There are systematic differences in the average

scattering properties of mare and highland units. At 13 cm wavelength mare surfaces are well modeled by a uniform dielectric with relative dielectric constant $\epsilon = 3.1$. Deviations from the value at this wavelength with the units studied thus far are small, on the order of 10%. At 116 cm the mare have considerable variation in inferred reflectivity. While much of the surface can be well matched by uniform dielectric models similar to that at 13 cm wavelength, there are also considerable deviations from that model. No simple model, consisting of a uniform dielectric interface or a contiguous set of such interfaces will match the data. Some type of frequency dispersive mechanism, such as layering and lossy dielectric is required. Highlands units in the Palus Somni, and Mare Crisium rim area possess lower effective dielectric constant than the mare. At 116 cm wavelength the data in this area are well modeled by uniform dielectric interface with relative dielectric constant $\epsilon = 2.8$. At 13 cm wavelength it has not been possible to find the simple model for the interface in this area. In the Apennines, at approximately 25° incidence, both 13 and 116 cm data show a reduction in reflectivity consistant with a change in relative dielectric constant from $\epsilon = 3.1$ to $\epsilon = 2.8$. Similar results are obtained in the central highlands.

Lunar rms slopes and slope distributions inferred from the radar data also show considerable variation with probing wavelength and topography. The systematic differences between mare and highlands are even stronger. At 13 cm, highland rms slopes vary approximately between

tan 6° and tan 8°, while in the mare this range of variation is approximately tan 2° to tan 4°. At 116 cm, highland rms slopes nearly equal those of the shorter wavelength, but within the mare the 116 cm slopes tend to be very nearly one-half as large as the 13 cm values at the same location. Evidently the small scale roughness is greater in the mare than that in the highlands. Changes in the rms slopes within the mare are a sensitive indicator of changes in terrain types. In some cases, such changes may be interpreted as occurring at flow contacts, or between geological units of different age or history.

In forward scatter, the unpolarized part of the 13 cm radar echo is generally insensitive to lunar topography. Variations in the unpolarized part are small and apparently without the systematic behavior among units evidenced by the polarized part. At 116 cm, there are significant variations in the unpolarized power and scattering law, but these variations are not associated with large scale lunar topography in an obvious manner. Chance observations of several craters that are prominent backscatterers in this wavelength range indicate that conversion of polarization state is primarily responsible for enhancement of the depolarized backscatter radar echoes...."

The data have demonstrated:

1. A strong wavelength dependence in the oblique scattering properties of the lunar surface in the decimeter to meter wavelength range;

2. Systematic differences in average scattering properties at a single wavelength of mare and highland units.

3. Variations in lunar surface structure with depth within mare units;

4. Systematic differences in lunar surface shape, as expressed by variation in lunar rms slopes with wavelength and between mare and highland units;

5. The presence at 13 cm wavelength of a diffuse scattering component that is essentially constant over the lunar surface;

6. The presence at 116 cm wavelength of a highly variable diffuse scattering component that is not correlated with obvious surface units.

These results have been given quantitative form and are described in the Preliminary Science Reports and in Tyler and Howard (1973). We believe that while significant results have been obtained, considerable work still remains.

In addition to the first order analysis techniques on which the foregoing conclusions were based, we have also developed techniques for extracting detailed slope frequency distributions from bistatic radar data (Parker and Tyler 1973). Preliminary results from this type of analysis are given in the paper just referenced, and in the Apollo 17 Preliminary Science Report (Moore and Tyler 1973). This technique provides a powerful method for examining subtle variations in the geologic texture of the lunar surface. A further outgrowth of this work is the ability to derive quantitative measures of the three dimensional distribution of scattered power in a particular scattering area.

We have also undertaken joint efforts with other investigators, principally Henry Moore of the USGS, Menlo Park, and T. W. Thompson of the Jet Propulsion Laboratory, Pasadena. An object of this collaboration was to carry out detailed studies of certain lunar surface features, for example Mare Serenitatus, using available data from a broad range of remote sensors and Apollo observations. Toward this end, a common

data file has been created at Stanford and the USGS in Menlo Park. At present, this file contains the dual frequency bistatic radar observations and an independently derived geologic interpretation of the lurrain for each bistatic radar data point. We intend to incorporate other observations, such as infrared eclipse temperatures, terrestrial backscatter radar maps, and lunar color differences, into this data file.

Beyond these preliminary results the Apollo data have provided the basis for a considerable advance in radar studies of the moon. The lunar surface is well resolved, the data are of high signal-to-noise ratio, and the theory of forward scatter from rough surfaces is sufficiently well understood to permit detailed inferences regarding the properties of the lunar surface in the scattering region. Except near the sub-earth point such inferences cannot be drawn from earth based radar observations because of the much more complex nature of the radar backscattering process at oblique incidence. Lunar rms slopes, slope frequency distributions, effective surface reflectivity, and the wavelength dependence of these quantities have been obtained from the Apollo data. But further work is required to bring these results into focus with the lunar problem as a whole.

As mentioned previously, the analyses carried out thus far have dealt with the global nature of the bistatic radar data. That is, the data have been analyzed in terms of their average variations with earth, moon, and spacecraft geometry. Large scale lunar features such as mare and terra units have been taken into account in the analysis and interpretation, but the primary aim of the work has been to describe the

properties of the moon as a whole. The techniques used to date are also suitable for studies of more detailed lunar surface features. In addition, there are certain aspects of the data that are not completely understood but where we can expect progress. We have proposed that this work be continued under the Lunar Analysis and Synthesis Program.

V. Conclusion

While we have concentrated here on the scientific results of S-170, we wish to emphasize that most of our efforts over the period of the contract have been involved in the technical process of collecting and reducing the data. These efforts are described in considerable detail in the NSSDC Report submitted with this report. The interested reader is referred to it for information regarding the nature of these efforts.

Over the period of this contract we were privileged to work with a large number of individuals at JSC and within other NASA organizations. We wish to comment positively here on the generally high caliber of the personnel with whom we worked. We wish to make special note of the helpfulness and cooperation of three individuals, Louis Leopold of the Electromagnetic Systems Branch, Patrick Lafferty of the Science and Applications Directorate and Harley Weyer of Flight Operations. Their roles were vital to the success of this experiment.

In general, we feel that this experiment has been highly successful. It has resulted in a distinct contribution to the radar astronomy art and a unique lunar data set. We have established certain results regarding

the nature of the lunar surface as a whole. Our remaining tasks are to extend this work to the study of specific lunar features, in collaboration with our geological colleagues, and to apply the technique to other celestial bodies.

VI. Bibliography

Tyler, G. L., Simpson, R. A., and Moore, H. J., "Lunar Slope Distributions: A Comparison of Bistatic Radar and Photographic Results," J. Geophys. Res., vol. 76, no. 11, pp. 2790-2795, April 1971.

Tyler, G. L. and Simpson, R. A., "Bistatic Radar Measurements of Topographic Variations in Lunar Surface Slopes with Explorer XXXV," Radio Science, vol. 5, no. 2, pp. 263-271, February 1970.

Tyler, G. L., "Oblique-Scattering Radar Reflectivity of the Lunar Surface: Preliminary Results from Explorer 35," J. Geophys. Res., vol. 73, pp. 7609-7620, December 1968.

Tyler, G. L., Eshleman, V. R., Fjeldbo, G., Howard, H. T., and Peterson, A. M., "Bistatic Radar Detection of Lunar Scattering Centers with Lunar Orbiter I," Science, vol. 157, no. 3785, pp. 193-195, July 1967.

SU-SEL-73-006

STANFORD APOLLO BISTATIC-RADAR EXPERIMENT (S-170): NATIONAL SPACE SCIENCE DATA CENTER DATA DESCRIPTION

February 15, 1973

G. L. Tyler
H. T. Howard
G. R. Dow

Technical Report No. 3282-1

Prepared under

National Aeronautics and Space Administration
Contract NAS 9-10579

Center for Radar Astronomy
Stanford University
Stanford, California 94305

Contents

13

Introduction

The Stanford Apollo Bistatic-Radar Experiment (S-170) was carried out during the lunar orbit phase of the Apollo 14, 15, and 16 flights. The experiment was unique in that no special equipment was placed onboard the Apollo vehicles and carried to the moon, and that the principal observations were carried out on the ground. Radio-frequency transmissions from the orbiting command-service-module were directed toward the moon and received on the earth after reflection from the lunar surface. Two wavelengths, 13 cm (2287.5 MHz, S-band) and 116 cm (259.7 MHz, VHF), were used. The best data were obtained during periods when the spacecraft was maneuvered to maintain a predetermined, although changing, attitude with respect to the earth and moon. During these periods, data were obtained at the two wavelengths simultaneously. Data were also obtained at the 116 cm wavelength during periods of inertial hold and SIM bay attitude maneuvers. Data reception took place at two sites on the earth, the NASA-DSN 64 m antenna facility located near Barstow, California and the Stanford Research Institute/ Stanford University 46 m antenna facility located on the campus of Stanford University, Stanford, California. The NASA facility was used for reception of the 13 cm data, the Stanford facility for the 116 cm data. In both cases the elements of the receiving system critical to the experimental objectives were under direct control of the experimenters. At the DSN, a Signal Conditioning Unit designed and constructed at Stanford was inserted as a critical series element in the data receiving system and used to set system bandwidths, levels and timing information for the analog recording system. Input signal levels, bandwidths, and

frequencies to the Signal Conditioning Unit from the DSN were specified and monitored in real-time during data collection by the experimenters. Data reduction was carried out at the Stanford Sigma 5 Real-Time Computation Facility. With two exceptions (cf. Notes on Block Diagram I, 4d, and Appendix V) identical programs and procedures were used for 13 cm and 116 cm data. Also, with one exception, the same programs were used for all three flights (cf. Subtask 2). However, certain parameters, defined elsewhere in the report, were varied for data at the two wavelengths.

Good data were obtained from the three flights. In the data sets accompanying this report we include the simultaneous 13 cm and 116 cm observations, but not the 116 cm data obtained in the inertial hold and SIM bay attitudes. Data are given in two forms:

a) A complete set of observations reduced to short time averages of the electromagnetic wave spectra for the 13 cm and 116 cm observations. These observations have been corrected for instrumental effects, and are unedited. Tapes containing these data are referred to as JM Doptrack tapes. The observations have been merged with trajectory data obtained from the Manned Space Flight Center in Houston, and certain ancillary data computed from the trajectory.

b) A complete set of reduced data records, called Integral tapes, obtained from the JM Doptrack tapes, which describe certain properties of the JM Doptrack data, such as moments of the echo spectra, and inferred properties of the lunar surface, such as rms slopes.

There is one-to-one correspondence between the Integral data and the JM Doptrack data; an interested investigator may use either the reduced data records given on the Integral tapes, or use the JM Doptrack tapes to verify the reduction procedure and perform additional reductions.

The remainder of this report describes the data collection and reduction system in some detail, attempts to give cautioning notes to

the data user, and describes the tape contents and formats for JM Doptrack and Integral tapes. However, no particular attempt to explain the motivation for the overall data reduction procedures will be made, except as it affects individual steps not described elsewhere. A more general understanding of the experiment, its goals, limitations, and preliminary results may be obtained from the references listed below:

Howard, H. T. and G. L. Tyler, "Bistatic-Radar Studies of the Lunar Surface," Apollo 14 Preliminary Science Report, NASA publication SP-272, 1971.

Howard, H. T. and G. L. Tyler, "Bistatic-Radar Investigation," Apollo 15 Preliminary Science Report, NASA publication SP-289, p. 23-1, 1972.

Howard, H. T. and G. L. Tyler, Apollo 16 Preliminary Science Report, NASA publication SP-315, p. 25-1, November, 1972.

Tyler, G. L. and H. T. Howard, "Bistatic Radar Observations of the Lunar Surface with Apollos 14 and 15," paper presented at Third Lunar Science Conference, Houston, Texas, January, 1972.

Tyler, G. L. and D. H. H. Ingalls, "Functional Dependence of Bistatic Radar Frequency Spectra on Lunar Scattering Laws," J. Geophys. Res., Vol. 76, No. 20, pp. 4775-4785, July, 1971.

16

Synopsis of Observations

A synopsis of the observations included with this report is given in Table I, "Stanford Apollo Bistatic-Radar Experiment Parameters." The definitions of the columns in Table I are given below:

SPACECRAFT - Designation of flight number

ORBIT - NASA-MSC orbit numbers, counted from lunar orbit insertion

WAVELENGTH - Either 13 cm or 116 cm, wavelength of electromagnetic radiation from command-service-module, corresponds to frequencies 2287.5 MHz and 259.7 MHz respectively.

ANTENNA - Command-service-module antenna in use. Quantities in ( ) are NASA-MSC designation. Antenna patterns used in data reduction obtained from NAA (1966a, 1966b, 1969), and MSC (1967). Apollo 14 experiment required compromise in spacecraft attitude to accomodate patterns from two fixed antennas.

3 db BEAMWIDTH - One-half power antenna beamwidths

POLARIZATION - Of command-service-module antenna

GAIN - Command-service-module antenna gain

POWER - Transmitted power, from command-service-module

SYSTEM TEMPERATURE - Equivalent temperature of receiving system on the earth, looking at cosmic background radiation perpendicular to plane of galaxy.

17

TABLE I

Stanford Apollo Bistatic-Radar Experiment Parameters

SPACECRAFT	ORBIT	WAVELENGTH	ANTENNA	3 db BEAMWIDTH	POLARIZATION	GAIN[β]	POWER[γ]	SYSTEM TEMPERATURE[δ]
Apollo 14	25	13 cm	Cavity backed helix (OMNI C)	~60°	Right elliptical axial ratio ~7 db	-1.5 db	~4 W	27°K ± 3°
Apollo 14	25	116 cm	Scimitar (VHF LEFT)	α	Linear, maintained in plane of incidence	~0 db	~2.5 W	~1000°K ± 50°
Apollo 15	28	13 cm	Steerable crossed dipoles (HIGH GAIN, WIDE)	~40°	Right circular axial ratio ≲1.0 db	-1.5 db	~4 W	27°K ± 3°
Apollo 15	28	116 cm	Scimitar (VHF RIGHT)	α	Linear, varies with respect to plane of incidence	~0 db	~2.5 W	~1000°K ± 50°
Apollo 16	40	13 cm	Steerable crossed dipoles (HIGH GAIN, WIDE)	~40°	Right circular axial ratio ≲1.0 db	-1.5 db	~4 W	27°K ± 3°
Apollo 16	40	116 cm	Scimitar (VHF LEFT)	α	Linear, maintained in plane of incidence	~0 db	~2.5 W	~1000°K ± 50°

α beamwidth of scimitar not defined
β includes circuit losses, nominal values ± 3 db
γ in carrier signal, nominal values, actual values not measured in flight
δ varies with orbital position of spacecraft, cold sky values given

Data Collection, Processing, Reduction

Block Diagram I, located at the rear of the report, depicts the flow of data through collection, processing, and reduction. Annotations and notes (circled numbers) give brief comments or descriptive titles as guides for reference. The overall data flow is divided into 11 subtasks, indicated by horizontal brackets. The remainder of the report is subdivided according to the subtasks. It is assumed that the reader has general familiarity with analog-to-digital and digital techniques for data reduction and analysis. Critical data reduction parameters are given in Table II and antenna parameters are given in Tables III and IV.

Each subtask description provides a general explanation of that subtask function. An attempt has been made to maintain independent description, with minimum reference to other functions. Highly technical details, such as magnetic tape formats and coordinate descriptions, are reserved for the appendixes. In this way a careful reading of the subtask descriptions, in connection with Block Diagram I, should provide a good overview of the data reduction process. The appendixes may be read at a later time, or for details.

A THOROUGH STUDY OF BLOCK DIAGRAM I PRIOR TO THE USE OF REPOSITORY DATA IS VERY HIGHLY RECOMMENDED.

TABLE II

STANFORD APOLLO DUAL-FREQUENCY BISTATIC-RADAR DATA SUMMARY

	APOLLO 14		APOLLO 15		APOLLO 16	
	116 cm (VHF)	13 cm (S-BAND)	116 cm (VHF)	13 cm (S-BAND)	116 cm (VHF)	13 cm (S-BAND)
Julian Ephemeris Day (00:00 UT2 Preceding Data)	2440988.5		2441164.5		2441430.5	
Reference Epoch for Coordinate Systems	2440952.509		2441317.752		2441317.752	
CALENDAR DATE	February 6, 1971		August 1, 1971		April 23, 1972	
Orbit Number (From Lunar Orbit Insertion)	25		28		40	
Transmitter Frequency	259.7 MHz	2287.5 MHz	259.7 MHz	2287.5 MHz	259.7 MHz	2287.5 MHz
UT2 START/STOP TIME	06:37:17/07:30:34	06:38:30/07:32:28	01:23:00/02:23:58	01:16:30/02:29:00	01:16:30/02:16:26	01:17:00/02:27:05
Spacecraft Antenna (MSC Designation)	VHF LEFT	OMNI C	VHF RIGHT	HIGH GAIN (WIDE)	VHF LEFT	HIGH GAIN (WIDE)
High Gain Antenna Pointing Angles						
α	-	-	-	144.°	-	145.°
β	-	-	-	122.°	-	302.°
Data Source	Stanford 10.003 MHz i.f. rcvr	DSN/STANFORD Closed Loop rcvr	Stanford 10.003 MHz i.f. rcvr	DSN/STANFORD Closed Loop rcvr	Stanford 10.003 MHz i.f. rcvr	DSN/STANFORD Closed Loop rcvr
Receiver Bandwidth	~3.5 kHz	~20.0 kHz	~3.5 kHz	~20.0 kHz	~3.5 kHz	~20.0 kHz
Data Sampling Frequency	10.0 kHz	43.0 kHz	10.0 kHz	43.0 kHz	10.0 kHz	43.0 kHz
Total Analysis Bandwidth	5.0 kHz	21.5 kHz	5.0 kHz	21.5 kHz	5.0 kHz	21.5 kHz
N, Number of Analysis Bins	1024	1024	2048	1024	2048	1024
Analysis Resolution	9.8 Hz	42.0 Hz	4.9 Hz	42.0 Hz	4.9 Hz	42.0 Hz
Length of Data Window/Transform	0.1024 sec.	0.02381395 sec.	0.2048 sec.	0.02381395 sec.	0.2048 sec.	0.02381395 sec.
L, Number of Transforms Averaged per JM Record (see Subtask 4)	26	100	23	99	23	99
Frame Length	2.6624 sec.	2.381395 sec.	4.7104 sec.	2.357581 sec.	4.7104 sec.	2.357581 sec.

TABLE III

Stanford Research Institute 46 m Antenna Performance (116 cm)

Aperture	Efficiency	Feed System	Mount	Pointing Loss
46 m dia.	~35% ±5%	Crossed dipole array axial ratio ~1. db ± 0.5[α] isolation ~16 db ± 1.0	el/az	< 0.1 db

TABLE IV

NASA DSN 64 m Antenna Performance (13 cm)*

Aperture	Efficiency	Feed System	Mount	Pointing Loss
64 m dia.	58% ±4%	Waveguide horn axial ratios ≲ 0.8 db[β] isolation ≳ 26 db[γ]	el/az	< 0.03 db

2

α estimated

β, γ Private communication, D. Bathker, JPL, 1973.

* DSN, 1972

Subtask 1

Data Collection

a) 116 cm. A detailed block diagram of the 116 cm receiver is given in Appendix I. The receiver is a superheterodyne of standard design. An unusual feature of this system is the summed second local oscillator signal used to produce offset 9.0 and 10.003 MHz intermediate frequency signals. In operation, the 10.003 MHz channel was tuned to the downlink signal carrier and its accompanying echo, while the 9.0 MHz channel was tuned to the subcarrier signal displaced $\pm$ 31.6 KHz from the 259.7 MHz carrier. This procedure was adopted to provide frequency dispersive redundancy against locally generated interference at the main carrier frequency. The receiver passband characteristics are given in Appendix III. However, all data given here were obtained through the main 10 MHz channel. Receiver outputs were multiplexed with standard frequency references and clock signals and recorded on analog tape. Parameters of the Stanford Research Institute 46 m dish are given in Table III.

(b) 13 cm. A detailed block diagram of the 64 m 13 cm receiving system is given in Appendix II. Again, standard superheterodyne techniques are employed. All 13 cm data were obtained from a phase-locked loop signal tracking system using manual tracking when the direct signal dropped below threshold of the phase-locked loop. The receiver passband characteristics are given in Appendix III. The NASA-DSN station configuration for this experiment is given elsewhere (DSN, 1970, 1971). Again, analog signals from the receiver output multiplexed with clock and reference frequencies were recorded. Parameters of the NASA DSN 64 m dish are given in Table IV.

22

Subtask 1 (cont.)

(c) Critical Bandwidths. Appendix III gives the power spectral densities obtained at the receiver outputs for the three Apollo experiments with uniform power spectrum (white) noise input. These curves were obtained in Subtask 4, and were used in the data normalization. For the 116 cm system additional checks made with coherent signals within $\pm$ 5 MHz either side of the 10 MHz intermediate frequency and within $\pm$ 20 MHz of the first intermediate frequency verified the absence of spurious responses that would not be detected by the noise calibration technique. Similar tests have been carried out by the DSN and the experimenters at the 64 m facility. Thus, the curves in Appendix III accurately represent the receiver response to signals near the frequency to which the receivers were tuned. Image rejection in the 116 cm system was greater than 100 db.

Subtask 2

Sampling

Data sampling was carried out using standard techniques on the Stanford Sigma 5 Real-Time Computation Facility. Right circular and left circular polarization signal channels were sampled simultaneously in synchronism with the multiplexed time reference signals. Sampling was initiated at the start of an even 10 sec. interval (UT2) by a start pulse derived from the recorded time code. The sampling programs were improved between the Apollo 15 and 16 experiments to obtain higher playback rates for the 13 cm data (see Block Diagram I, Notes, 4d). With this exception, the same computer programs were used for data reduction from the three sets of observations. A small overlap was provided between subsequent sample data tapes. These overlaps were carried through the remainder of the data processing. Tape recorder playback levels were adjusted for equality between left circular and right circular polarization using the controlled reference signal levels for calibration. The playback recorder electronics were equalized for the particular tape source (FR1400 A, FR1400 B, HP3955B) prior to sampling data from that source. Output from the data sampling process was stored on magnetic tape. The quantization level was 8 bits. The i^{th} data sample generally will be denoted $\hat{d}_i$: data from the left circularly polarized antenna ${}_1\hat{d}_i$, data from the right circularly polarized antenna ${}_2\hat{d}_i$.

24

Conversion to Frequency Domain

All data have been rendered in the frequency domain in the form of modified complex Fourier coefficients (Blackman and Tukey, 1958). A sequence of data samples was multiplicatively weighted with a sine-squared (Hanning) data window and then Fourier analyzed using fast Fourier transform techniques. Analytically, the data samples were grouped, separately for each polarization, according to

$$d_j^n = \hat{d}_i, \qquad (1)$$

where $i = nN + j$, $j \leq N$; n,N,j positive integers or zero. The modified complex Fourier coefficients are

$$f_k^n = \sum_{j=o}^{N-1} \sin^2\left(\frac{2\pi}{N} j + \frac{\pi}{N}\right) d_j^n \, e^{-i(2\pi/N)jk}, \qquad (2)$$

where $i = \sqrt{-1}$, $0 \leq k \leq N-1$. In the Apollo data reduction programs, N was either 1024 or 2048 (see Table II). Each set of coefficients corresponds to a time interval T = N·(sampling interval) (see Table II for values). The outputs of the transformation are the f_k^n above.

Subtask 4

Generation of Coherency Matrix

The coherency matrix (Born and Wolf, 1959) was determined directly from the f_k^n by forming the summed products

$$\begin{bmatrix} \sum_{n=1}^{L} |{}_1f_k^n|^2 & \sum_{n=1}^{L} {}_1f_k^n \; {}_2f_k^{n*} \\ \sum_{n=1}^{L} {}_1f_k^{n*} \; {}_2f_k^n & \sum_{n=1}^{L} |{}_2f_k^n|^2 \end{bmatrix} \tag{3}$$

where * denotes complex conjugate. Each sum is a function of the frequency index k. In order to compensate for the non-uniform effects of the receiving system filters, we further form

$${}_1\hat{q}_k^2 = \langle {}_1q_k^2 \rangle = \sum_{n=1}^{M} |{}_1q_k^n|^2$$

$$\tag{4}$$

$${}_2\hat{q}_k^2 = \langle {}_2q_k^2 \rangle = \sum_{n=1}^{M} |{}_2q_k^n|^2$$

where $q_k^n = f_k^n$ for periods with signal absent. The $\hat{q}_k^2$ are the receiving system output power spectra for a noise input. The upper bound M was chosen to reduce the fluctuations in $\hat{q}_k^2$ to a small value. Typically $M \tilde{<} 10^4$, for which $\hat{q}_k^2$ is determined to approximately one percent. The coherency matrix, corrected for receiver power transfer characteristics is

$$\underline{J}_k = \begin{bmatrix} J_{11} & J_{12} \\ J_{21} & J_{22} \end{bmatrix}, \tag{5}$$

26

Subtask 4 (cont.)

where

$$J_{11} = \frac{1}{{}_1\hat{q}_k^2} \sum_{n=1}^{L} |{}_1f_k^n|^2$$

$$J_{22} = \frac{1}{{}_2\hat{q}_k^2} \sum_{n=1}^{L} |{}_2f_k^n|^2 \qquad (6)$$

$$J_{12} = \frac{1}{{}_1\hat{q}_k \, {}_2\hat{q}_k} \sum_{n=1}^{L} {}_1f_k^n \; {}_2f_k^{n*}$$

$$J_{21} = J_{12}^* \, .$$

The fractional polarization of the received signal may be computed directly from the $\underline{J}_k$ as

$$\gamma_k = \left\{ 1 - \frac{4 \text{ Det } \underline{J}_k}{\text{Trace}^2 \, \underline{J}_k} \right\}^{1/2} . \qquad (7)$$

Again γ_k is a function of the frequency index k. The output of Subtask 4 consists of the spectra $\underline{J}_k$, γ_k. The parameters L and N used in the reduction of the several sets of observations are included in Table II. Completion of the $\underline{J}_k$ (Subtasks 2, 3, and 4) represented the greatest portion of the computational expense for this experiment. Additional results may be obtained directly from $\underline{J}_k$ and γ_k. For example, the power in the polarized and unpolarized parts of the echo is:

27

Subtask 4 (cont.)

$$\text{polarized power} \qquad P_p(k) = \gamma_k \cdot \text{Trace } \underline{J}_k$$

$$\text{unpolarized power} \qquad P_u(k) = (1-\gamma_k) \cdot \text{Trace } \underline{J}_k \,. \tag{8}$$

Other parameters of the echo spectra may be obtained similarly (Born and Wolf, 1959; Appendix 10).

28

Subtask 5

Correction for System Polarization Parameters

The quantities $\underline{J}_k$ and Y_k discussed in the previous section under Subtask 4 were derived directly from the sample data as they came from the analog tapes. As discussed under Subtask 4 certain corrections have been made for the receiver filter characteristics. However, the data were treated as though they were derived from perfect antennas. That is, the antennas were assumed to consist of a pair of right and left circularly polarized elements. It was further assumed that, with the exception of the filter corrections already applied, the gains in the two receiver channels were equal. In the case of the 13 centimeter data this assumption was very good. The isolation of the DSN 64 m antenna has been measured as > 26 db with an axial ratio of $\tilde{<} 0.8$ db (private communication, D. Bathker, JPL, 1973). At 116 cm the properties of the SRI 46 m antenna are not nearly so well known. Polarization of the 46 m antenna was controlled principally through the constraints applied to the construction of the feed system. The feed system consisted of a crossed dipole array of linear elements connected through a standard hybrid to obtain a circular polarization. The array elements were mechanically and electrically identical. The hybrid combiner and associated phase shift elements were adjusted to within 1^{o} and 1 db of the ideal transfer function for such a device. Coupling between the orthogonal linear array elements was less than 40 db with the feed removed from the dish. Cross-coupling between the two circular polarizations, observed at the hybrid output with the feed in place at the focus of the dish, was 16 db. We were unable to measure the axial ratio of the overall system with the feed in place in the dish. We estimate axial ratio of the 116 cm system as approximately 1 db for either polarization. For certain received polarizations axial ratios

of this magnitude can introduce significant errors in the calculation of fractional polarization. Consequently, a correction for this uncertainty was applied in Subtask 5. This correction was applied to the 116 cm Apollo 14 and 16 data only. The output tapes from Subtask 5 preserve the original $\underline{J}_k$ computed earlier.

The corrections were determined as follows (cf Tyler, 1970). Consider the signals arriving at the antenna terminals in terms of their right and left circularly polarized components, which we will denote E_r, E_l, respectively. The relationship between the arriving signals and the signals at the antenna terminals may be expressed as a matrix multiplication

$$\begin{bmatrix} E'_r \\ E'_l \end{bmatrix} = \begin{bmatrix} c_{11} & c_{12} \\ c_{21} & c_{22} \end{bmatrix} \begin{bmatrix} E_r \\ E_l \end{bmatrix} \qquad (9)$$

where the c's are complex and arbitrary. The matrix elements may be thought of as the transmission coefficients of the four port network consisting of pairs of antenna elements and terminals. Physically, the c's may represent attenuation, gain, and cross-coupling. In an ideal system $c_{11} = 1$, $c_{12} = c_{21} = 0$, $c_{22} = 1$.

The effect of such a transformation on the coherency matrix $\underline{J}$ is easily shown to be

$$\begin{bmatrix} J'_{11} \\ J'_{12} \\ J'_{21} \\ J'_{22} \end{bmatrix} = \begin{bmatrix} |c_{11}|^2 & c_{11}c_{12}^* & c_{11}^*c_{12} & |c_{12}|^2 \\ c_{11}c_{21}^* & c_{11}c_{22}^* & c_{12}c_{21}^* & c_{22}^*c_{12} \\ c_{11}^*c_{21} & c_{21}c_{12}^* & c_{22}c_{11}^* & c_{22}c_{12}^* \\ |c_{21}|^2 & c_{22}^*c_{21} & c_{22}c_{21}^* & |c_{22}|^2 \end{bmatrix} \begin{bmatrix} J_{11} \\ J_{12} \\ J_{21} \\ J_{22} \end{bmatrix} \quad (10)$$

where $\underline{J}'$ is the coherency matrix of the wave associated with $\underline{J}$ observed at the antenna terminals. The k subscripts have been suppressed for convenience. However, it is assumed that the c's are independent of frequency over the spectrum of interest. Given $\underline{J}'$ and the c's, the original $\underline{J}$ may be recovered through an inverse matrix manipulation. In the present case $\underline{J}'$ is observed, but the c's are unknown.

The c's may be estimated from an observation of an unpolarized signal (Tyler, 1970). System noise inputs to the 116 cm receiver system were used to estimate the c's and perform a correction. The method was based on an experimenter selection of those portions of the receiver output spectrum that contained only receiver noise. If it is assumed that the noise input is unpolarized, then

$$\begin{aligned} J'_{11} &= (|c_{11}|^2 + |c_{12}|)^2 J_o \\ J'_{12} &= (c_{11}c_{21}^* + c_{22}^*c_{12}) J_o \\ J'_{21} &= J'^*_{12} \\ J'_{22} &= (|c_{21}|^2 + |c_{22}|^2) J_o, \end{aligned} \quad (11)$$

Subtask 5 (cont.)

where

$$J_o = k\,T_{sys}/2$$
$$k = 1.38 \times 10^{-23} \text{ (Joules/deg. Kelvin)} \quad (12)$$
$$T_{sys} = \text{system temperature.}$$

The signal will appear unpolarized if

$$J'_{12} = 0 \text{ and } J_{11} = J_{22}$$

or

$$c_{11}c_{21}^{*} = -c_{22}^{*}c_{12} \quad (13)$$

and

$$|c_{11}|^2 + |c_{12}|^2 = |c_{21}|^2 + |c_{22}|^2 ,$$

from which the required inverse transformation can be obtained. In practice, a numerical estimate of the correction matrix was obtained as described above. This estimate was then used as a starting point in a search to find the c's which minimized the apparent polarization of the corrected $\underline{J}'_k$ in the noise portions of the spectrum. The corrections in the form just described were then used to compute the corrected $\underline{J}'_k$ for the entire spectrum. A corrected fractional polarization γ'_k based on $\underline{J}'_k$ was then obtained.

The output tapes from Subtask 5 contain the <u>original</u> $\underline{J}_k$ and the <u>new</u>, <u>corrected</u> γ'_k. A data user may easily recompute the original γ_k from the $\underline{J}_k$ which have been preserved and which are available on the tapes supplied (see Subtask 6, Appendix IV). The correction factors employed in the generation of the γ'_k are given in Appendix VIII.

32

Subtask 5 (cont.)

In summary, steps in this subtask are:

a) Read $\underline{J}_k$ source tapes from Subtask 4

b) Determine elements of the correction matrix based on minimization of the polarized part of the noise.

c) Compute γ_k'.

d) Generate new tape containing the <u>original</u> $\underline{J}_k$ and <u>new</u> γ_k'.

This process was applied to the Apollo 14 and 16 116 cm data: 13 cm data are uncorrected, i.e., for 13 cm data $\gamma_k' = \gamma_k$. In subsequent steps the γ_k' were used in all computations of the polarized and unpolarized parts of the 116 cm echo spectrum.

Subtask 6

Merging Observations with Trajectory

The output of Subtask 5, the $\underline{J}_k$, γ'_k tapes, represents the experimenter's best estimate of the received spectra, averaged over the time intervals previously defined: that is, a complete second order description of the received echo signal. In the present step this data, which was previously processed without regard to lunar coordinates or other geophysical considerations, was combined with the Apollo command-service-module ephemeris. The emphemeris was first interpolated to the mid-point of the averaging period used in the computation of the $\underline{J}_k$, then certain ancillary quantities were computed. The interpolated ephemeris and the derived quantities were then merged with the experimental data to form a basic set of source tapes designated JM Doptrack. After further processing in Subtask 10, these tapes became the primary source tapes supplied with this report to the NSSDC.

The ephemeris based quantities added to the observational data were:

a) Time corresponding to mid-point of averaging period

b) Predicted difference between reflected and direct doppler shifts

c) Predicted echo bandwidth for a moon with rms slope of 0.1

d) Angle of incidence on mean spherical moon

e) Spacecraft altitude above mean spherical surface

f) Speed of the spacecraft

g) Bistatic-radar cross-section of a smooth, perfectly conducting, spherical moon for the current spacecraft-moon-earth geometry

h) Normalized signal strength for a conducting moon and instantaneous geometry

i) Spacecraft position in selenographic coordinates

j) Specular point position on a mean spherical lunar surface in selenographic coordinates

k) Selenographic latitude and longitude of spacecraft position

l) Doppler shift due to rotation of the earth

m) Total doppler shift of the reflected signal

n) Selenographic latitude and longitude of specular point on the mean spherical lunar surface

o) Speed of the specular point on the mean lunar surface

p) Look angles to earth in spacecraft coordinates

q) Euler angles of spacecraft attitude in local horizon system

r) Selenographic unit velocity vector of spacecraft

s) Selenographic unit vector location of earth.

These tapes are organized in groups of six data records, referred to as a data frame, corresponding to each time interval. A complete description of the JM Doptrack tape formats and contents is given in the appendixes (see Appendix IV).

Subtask 7

Computation of Polarized and Unpolarized Parts, Carrier Suppression

JM Doptrack tapes contain spectrally analyzed 13 cm and 116 cm receiver outputs. No provision was made within the receivers or Subtasks 2, 3, 4, 5, or 6 for removal of the directly propagating telemetry carrier from the echo data. In terms of the polarization parameters, this signal cannot be removed completely. However, much of the data analysis is based only on the low order moments of the polarized part of the echo. Subtask 7 computed polarized and unpolarized spectra from relation (8), Subtask 4, then used an empirically derived algorithm to remove the carrier signal from the polarized spectra; these data together with the ephemeris data described in Subtask 6 constitute the intermediate data set generated by Subtask 7. The algorithm for carrier suppression is described in Appendix V. Carrier suppression was also applied to unpolarized data. However, the carrier was largely suppressed in those data by coherency matrix processing, since it was a polarized signal. The output of this subtask, the P tapes, contain the experimenter's best estimate of the power spectra of the polarized and unpolarized components of the echo signal.

Subtask 8

Computation of Total Received Power, Echo Moments

Inputs to this subtask were the polarized and unpolarized power spectra derived from the JM Doptrack source tapes (Subtasks 6, 7). The purpose of Subtask 8 was to derive numerical measures of the echo spectra. Certain measures of the echo spectra were corrected for predictable trajectory effects and converted into scientific units. In all cases, the designation of the echo signal location in a spectrum was made by the experimenter's visually scanning plots of the polarized and unpolarized power spectra. The values of the k indices bounding the echo were input to a computer program that did the actual data reduction. An average noise level, determined from a region of the spectra not containing echo, was also input to the computer program. The data were monitored at approximately 30 sec. intervals and the echo limits reset to account for motion of the echo in the receiver passband. It was also necessary to occasionally reset the noise level as it also varied during the experiment, principally due to the scan of the receiving antenna across the lunar terminator. The derived quantities are given below:

a) Polarized echo power -- the integral of the polarized power spectra between the frequency limits set by the experimenter and above the system noise level. This quantity is the best measure of the polarized echo power received.

b) Normalized polarized echo power -- the quantity described in a) above, divided by the polarized system noise level.

c) Unpolarized echo power -- the integral of the unpolarized power spectra between the frequency limits set by the experimenter and above the system noise level. This quantity is the best measure of the unpolarized echo power received.

d) Normalized unpolarized echo power -- the quantity described in c) above, divided by the unpolarized system noise level.

e) Equivalent area bandwidth -- the bandwidth of the polarized echo signal between the frequency limits set by the experimenter and above the polarized system noise level as determined by the ratio of the total polarized echo power to the peak polarized echo power.

f) Normalized absolute moment bandwidth -- the bandwidth of the polarized power echo as described in e) above, computed from a gaussian equivalent absolute moment, and divided by e).

g) Normalized second moment bandwidth -- the bandwidth of the polarized power echo as described in e) above, computed from a gaussian equivalent second moment, and divided by e).

h) Centroid of echo spectrum -- the centroid of the polarized power echo as described in e) above.

i) RMS slope -- the rms slope of the lunar surface inferred from the value of e) above and the predicted bandwidth for an rms surface slope of 0.1, using linear interpolation.

Formulas for the computation of the above quantities and a brief explanation of their use may be found in Appendix VI. The trajectory data added in Subtask 6 were retained throughout this subtask. A simple correspondence between the output of this subtask and the JM Doptrack tapes was maintained through inclusion of ephemeris data in both data sets.

38

Subtask 9

Final Editing of Data

Final editing of the output from Subtask 8 resulted in a set of reduced data records designated Integral tapes. These tapes constitute the second form of data supplied to the NSSDC.

Final editing of data included the following steps:

a) Addition of hand-scaled bandwidths as a partial independent check on Subtask 8 (see Subtask 10).

b) Addition of spacecraft antenna gain in the direction of specular reflection.

c) Notation of operational or data processing changes

i) Polarized band bad

ii) Unpolarized data bad

iii) Change in polarized noise level

iv) Change in polarized k indices for echo limits

v) Change in unpolarized noise level

vi) Change in unpolarized k indices for echo limits

vii) Change in system gain

Caution: Some integral data, primarily at the beginning or end of a transmission, have been deleted. Large overlaps in the 13 cm data caused by the use of two analog tape recorders have also been deleted. In all other cases bad data, for example when interference is present, are flagged on the edited Integral tapes as described in c) above (see Appendix VI, E47). The data contained on the Integral tapes are still the experimenter's best estimates of the values. However, in the case of flagged data, that estimate may be very poor. No flagged data should be used without examining the spectra on the corresponding JM Doptrack tapes. For example, in the 116 cm data occasional interference produced marked increases in the apparent polarized echo power, but evidently left the unpolarized

power unaffected. A flag for polarized power thus may also cast suspicion on the unpolarized power. The experimenters have evaluated these cases and indicated their opinions accordingly in the data. Other individuals may arrive at different conclusions. It is primarily for this reason that the JM Doptrack/Integral tape frame-to-record correspondence (through ephemeris data) has been maintained: reduced data records on the Integral tapes may, if questioned, be re-evaluated from the JM Doptrack source tapes. A complete description of the Integral tape formats and the flags is given in Appendix VI.

Subtask 10

Displaying, Scaling, and Copying the Data

Output from Subtask 6, the JM Doptrack tapes, is used in miscellaneous programs in preparation for data analysis and distribution. An important step in producing the final Integral tapes (Subtask 9) took place here. Polarized power spectra obtained from JM Doptrack tapes are computer plotted and visually examined to determine specifically

a) proper receiver operation
b) proper receiver tuning
c) presence of interference.

Such plots are also used to determine the one-half power, hand-scaled bandwidths added to the data set in Subtask 9. This bandwidth is determined by measuring the width of the polarized echo spectrum at a point one-half the distance from the apparent system noise level to the mean echo peak. The measured distance is scaled by the appropriate factor to determine the width in Hertz. Such measures can be related to the rms slope of the lunar surface from the quasi-specular scattering theory (see Appendix VI). The hand-scaled values are used to verify the machine algorithms used in computing lunar rms slopes and as a simple means of quickly estimating the slope.

Finally, this subtask included copying of the JM Doptrack tapes for shipment to the NSSDC. These tapes were not edited.

Subtask 11

Utility Routines

Integral tapes have been organized as a sequence of records describing the data and experimental geometry at successive instances of time. It is then a simple matter to determine any set of variables from this tape with time as a parameter. We suggest that data users consider this data as a set of dependent functions parameterized in time and hope that such a presentation is found useful.

42

APPENDIX I

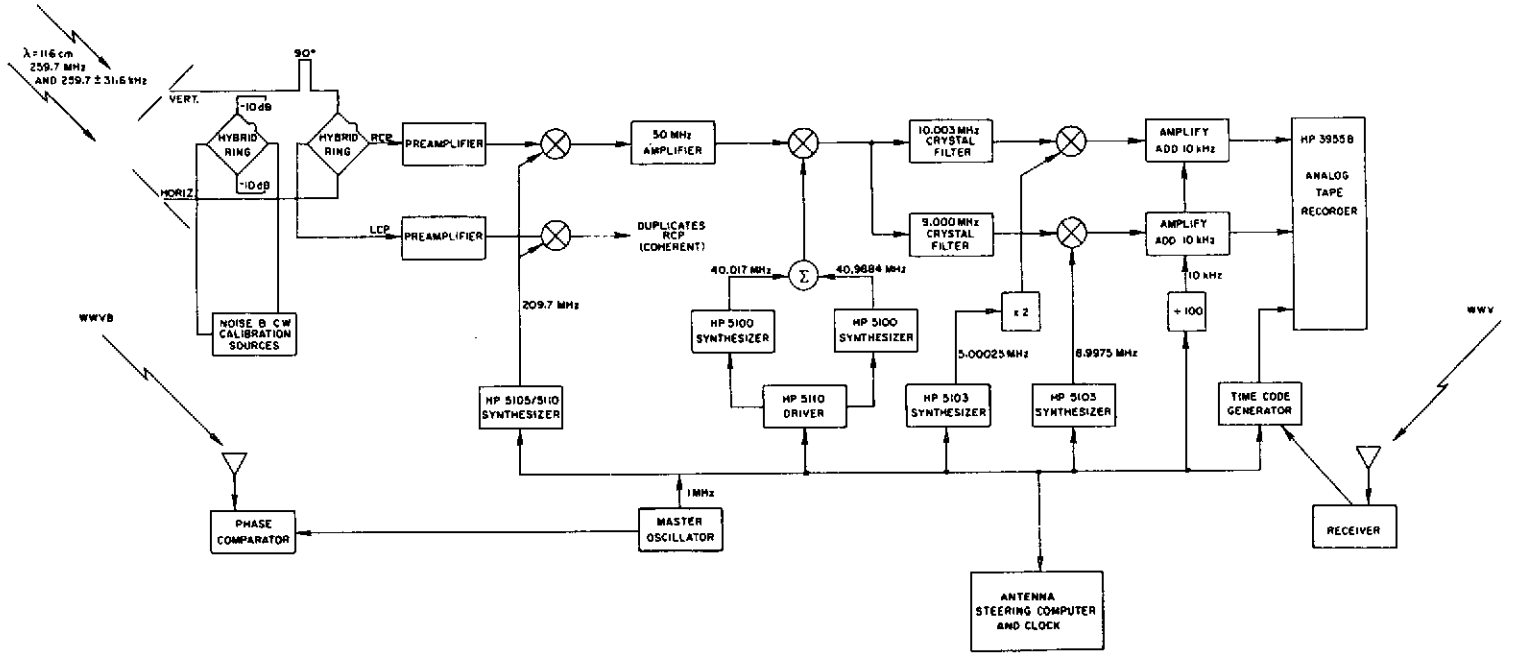

Stanford Apollo 116 cm (VHF) Bistatic-Radar Receiving System:
Major Elements

APPENDIX II

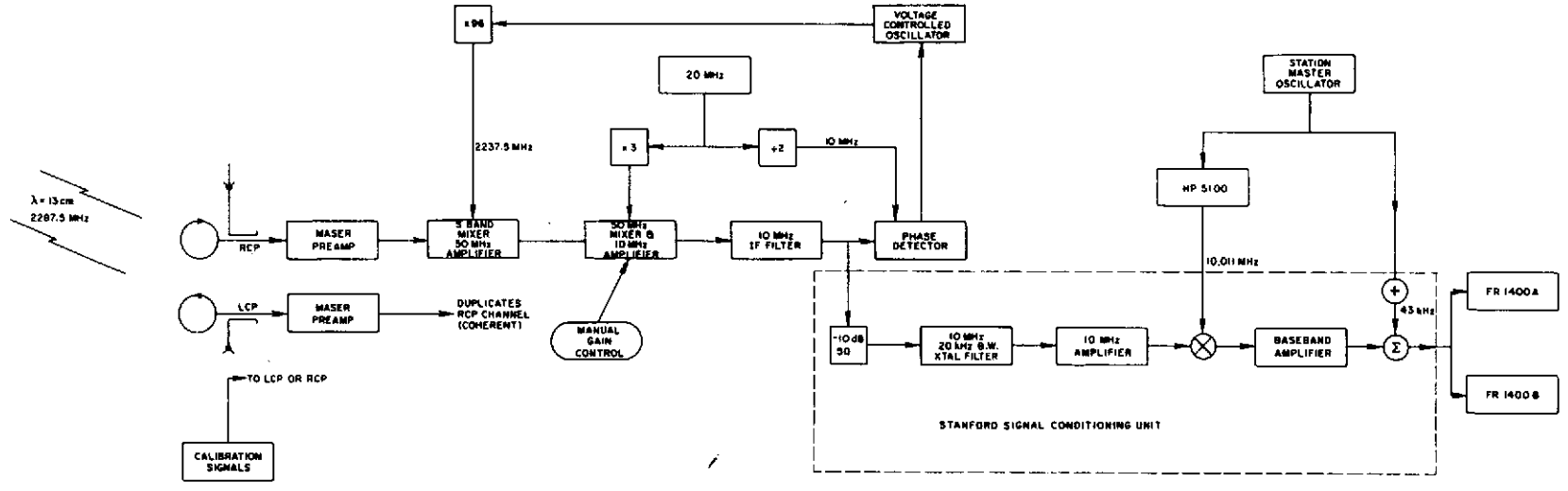

Stanford Apollo 13 cm (S-Band) Bistatic-Radar Receiving System:
Major Elements

APPENDIX III

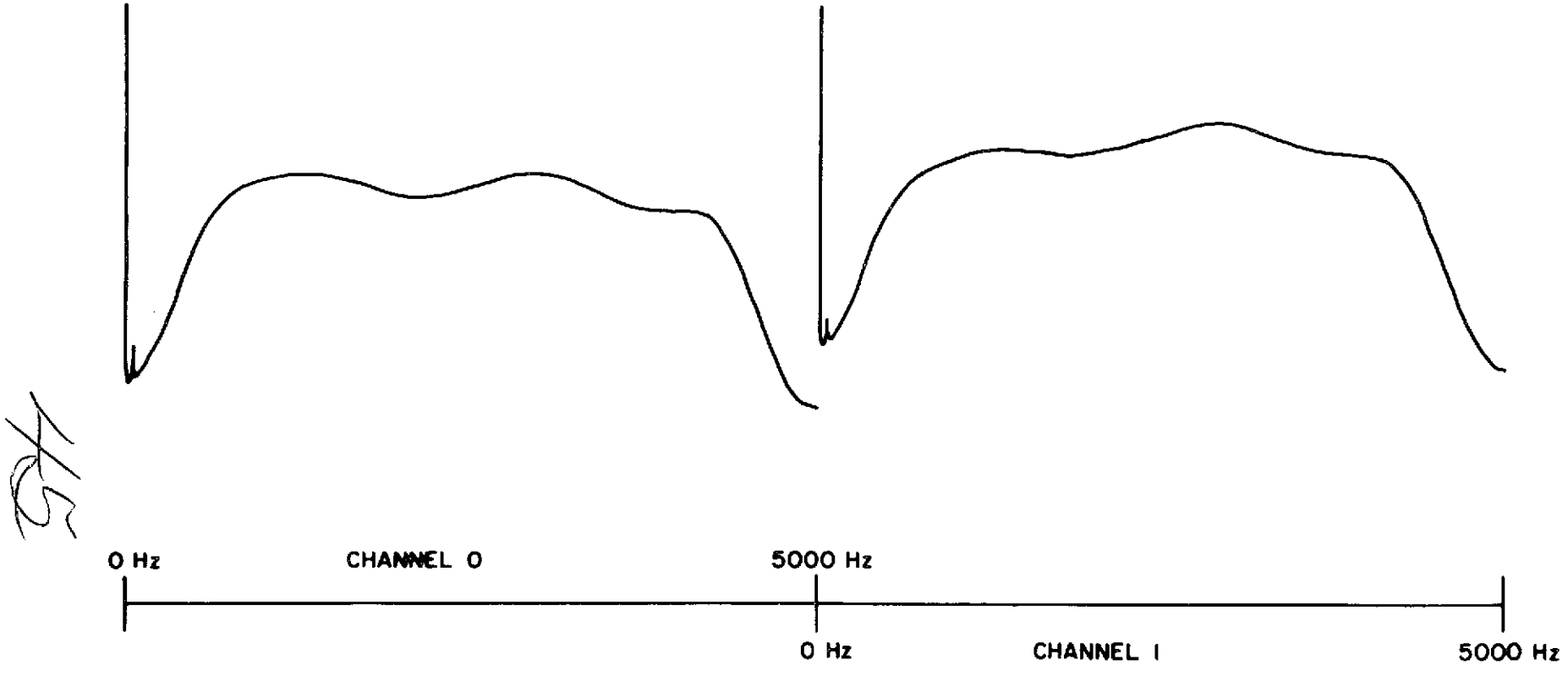

Apollo Bistatic-Radar Receiving System
116 cm Uncorrected Frequency Response

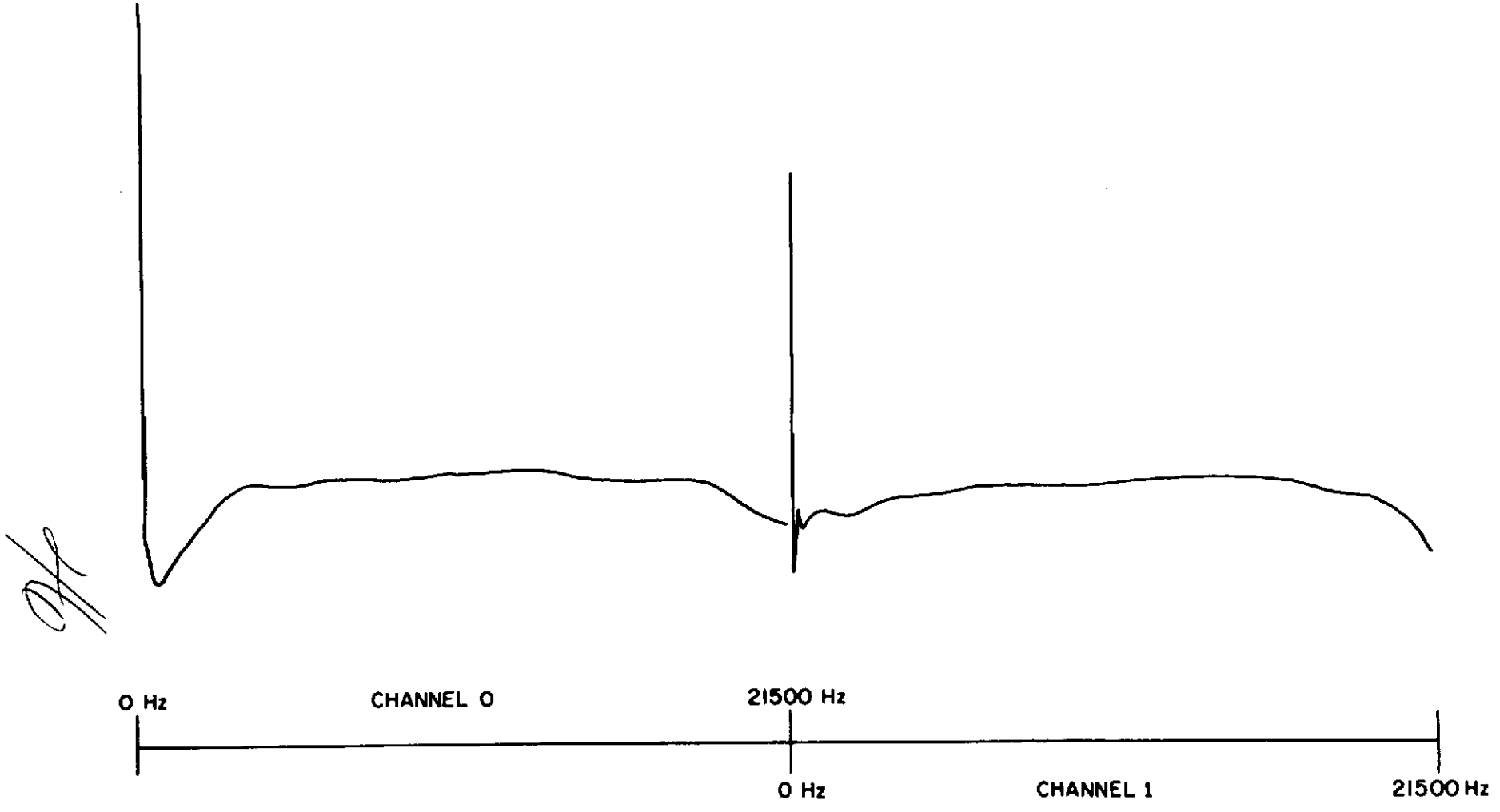

Apollo Bistatic-Radar Receiving System
13 cm Uncorrected Frequency Response

Appendix IV

JM Doptrack Tape Formats

This appendix describes the tape formats for the JM Doptrack Tapes generated in Subtask 6 of the text. Tapes are 9 track, binary in XDS Sigma 5 machine images[α]. These tapes contain the output of the polarimeter in Subtask 4, the corrected fractional polarization obtained from Subtask 5, MSC trajectory data, and certain ancillary quantities computed at Stanford. All records within the given file are the same length. There may be more than one tape per file. Files are identified by a header record which contains a brief description of the file contents. This appendix describes the tape organization, the file organization, and the record formats for the JM Doptrack tapes. Definitions of the tape contents are either given here or described by reference.

A. File Organization

File	No. Tapes	Contents	Record Length
1	1	Apollo-14 116 cm	514 words
2	1	Apollo-14 13 cm	514 words
3	1	Apollo-15 116 cm	1026 words
4	2	Apollo-15 13 cm	514 words
5	1	Apollo-16 116 cm	1026 words
6	2	Apollo-16 13 cm	514 words

B. File Organization

1. Header Record
2. Data Record 1
   Data Record 2
   Data Record 3 } Observational Data } Data Frame
   Data Record 4
   Data Record 5
   Data Record 6 Ephemeris Data
   ⋮
   < Many Data Frames >
   ⋮
3. EOF (End of File Mark)

[α]See Appendix XI for a description of Sigma 5 machine images.

47

If more than one tape was needed to contain the JM Doptrack file, the file was continued across the end of the tape to the next tape without interruption; there is only one header record per file, at the beginning of the first tape of the file.

Once again, even though the files are physically nothing more than a continuous string of records, all of equal length, it is helpful to think of them (see figure below) as being composed of a header record followed by groups (frames) of six records. The ephemeris data record concludes the frame and, since each JM data frame is a short-time average, the ephemeris data have been calculated using the midpoint of the frame as the instantaneous time reference point.

JM Doptrack File Containing N Data Frames

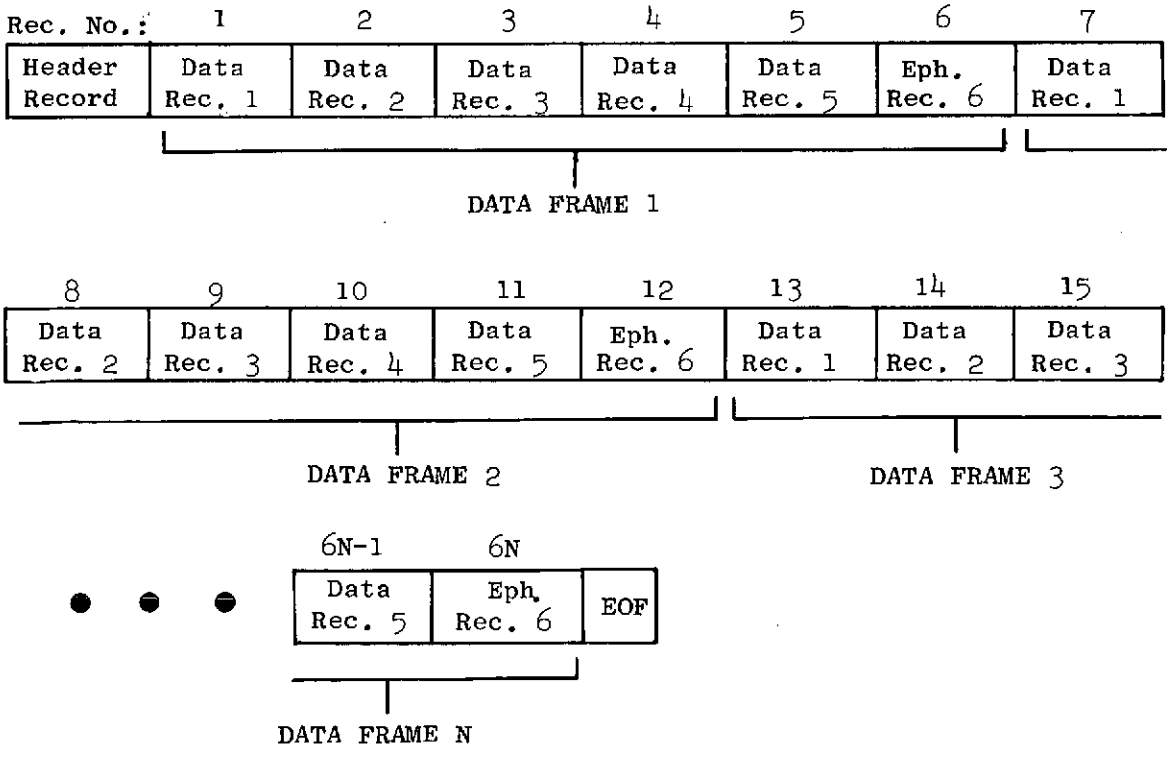

48

C. Header Record Formats

Word No.	Contents	Units	Machine Type[α]
1-42	Alphanumeric file identifier	--	A
43	Day of year on which data were collected (January 1 = 1)	(days)	I
44	Year data were taken (Gregorian)	(year)	I
45-46	Julian Ephemeris Day at 00:00 UT2 on the day the data were taken	(days)	DPR
47-48	Julian Ephemeris Day of reference epoch	(days)	DPR
49	Time increment between centerpoint of data averaging frame	(sec)	R
50	Number of data records following this header record (Number of data frames = number of data records divided by 6)	--	I
51-514/1026	Not used		

D. Data Frame Formats

1. Data Record Organization

Record No.	Contents
1	$J_{11}(k)$
2	$J_{22}(k)$
3	Real part of $J_{12}(k)$
4	Imaginary part of $J_{12}(k)$
5	$\gamma(k)$
6	Spacecraft ephemeris and ancillary data

Note:

116 cm data

$J_{11}(k)$ - Left circular polarization

$J_{22}(k)$ - Right circular polarization

13 cm data

$J_{11}(k)$ - Right circular polirization

$J_{22}(k)$ - Left circular polarization

[α] A - Alphanumeric
I - Integer
R - Real
DPR - Double Precision Real

49

D. 2. Format Records 1-5 (all machine type real)[ω]

Record No.	Contents
1-513/1025	Data described under D.1 above
514/1026	Meaningless

3. Format Record 6 (all machine type real)

Word No.	Contents	Units
1	Meaningless	
2	UT2 at midpoint of frame	(sec)
3	Reflected doppler minus direct doppler	(Hz)
4	Predicted bandwidth for rms surface slope of 0.1	(Hz)
5	Angle of incidence	(deg)
6	Spacecraft altitude (mean lunar radius assumed 1736 km)	(km)
7	Spacecraft speed	(m/sec)
8	Radar cross section predicted for smooth conducting moon	(dim)
9	(Radar cross section)/(received power)	(m^2/w)
10	X } Components of selenographic unit position vector of spacecraft location	(dim)
11	Y	
12	Z	
13	X } Components of selenographic unit position vector of specular point location	(dim)
14	Y	
15	Z	
16	Selenographic latitude of subspacecraft position	(deg)
17	Selenographic longitude of subspacecraft position	(deg)
18	Component of doppler shift due to earth rotation	(Hz)

[ω]Due to a hardware problem in the data processing, words 1-15 are zero in the Apollo-14, 116 and 13 cm, and Apollo-15 13 cm files.

50

D. 3. Format Record 6 (all machine type real) (cont.)

Word No.	Contents	Units
19	Total doppler shift of reflected signal	(Hz)
20	Selenographic latitude of specular point	(deg)
21	Selenographic longitude of specular point	(deg)
22	Speed of specular point on the lunar surface	(M/sec)
23	α_e } Vehicle look angles	
24	β_e } to earth	
25	θ } Euler angles of local	
26	Ψ } horizon coordinates	(deg)
27	φ }	
28	X } Spacecraft selenographic	
29	Y } unit velocity vector	(dim)
30	Z }	
31	X } Selenographic unit vector from center of	
32	Y } moon to center of	
33	Z } earth	(dim)
34-514/1026	Not used	

Note: Data do not always progress uniformly in time. Occasionally, data frames will reverse in time for one frame, and then continue forward. This effect is caused by the sampling procedure in which deliberate overlap was inserted. Time on data is correct.

E. Definition of Contents

1. Data -- defined under Subtasks 4 and 5 of the text.
2. Ephemeris and Ancillary Data -- described in greater detail in Appendix VI.

Appendix V

Carrier Suppression Algorithm

This appendix describes the algorithm used to remove the direct signal from the polarized and unpolarized parts of the bistatic-radar echo spectrum (see Subtask 7). This algorithm was used on each frame of polarized and unpolarized data which the JM Doptrack tapes yield according to relation (8), Subtask 4. Two slightly different procedures were used for the 116 cm and 13 cm data. These differences constituted the only difference in procedure between the 116 cm and 13 cm data. Both data sets were processed by the same computer program, with different program branches for the two cores. The direct signal observed at 13 cm was free of spurious sidebands to the level of our observations. At 116 cm, the direct signal contained two weak sidebands symmetrically displaced approximately 20 db below the direct signal. Consequently, during periods of strong direct signal at the 116 cm wavelength, it was also necessary to correct for the presence of these sidebands. The procedures described below were developed empirically but were found to give good results. The approach was to find the maximum of the power spectrum and to assume that this maximum represented the direct signal. This assumption was tested by determining the height of the maximum with respect to the fluctuations in the spectrum in the immediate vicinity of the maximum. If the maximum exceeded the fluctuation criteria then an interpolation procedure was used to provide a smoothed estimate of the spectrum. In the case of the 116 cm data, sideband suppression was achieved by reducing the local maximum on either side of the direct signal by an amount proportional to the strength of the direct signal. A detailed summary of this procedure is given below.

Initial Test

1. Find the absolute maximum of all the data, MAX (see figure which follows).
2. Find the adjacent local maxima, MAX12 and MAX34.
3. Test MAX to determine whether or not it represents the direct signal.

   i) $$SUM = \frac{MIN1 + MIN2}{8} + \frac{MAX12}{4} + \frac{MIN3 + MIN4}{8} + \frac{MAX34}{4}$$

52

Initial Test (cont.)

ii) CRIT = 1.2·SUM

iii) (MAX.LT.CRIT) ⇒ no direct signal present, terminate procedure; go to next frame, initial test 1.
(MAX.GE.CRIT) ⇒ direct signal present, continue.

4. Check data type. If data is 116 cm then go to step 8, otherwise continue with step 5.

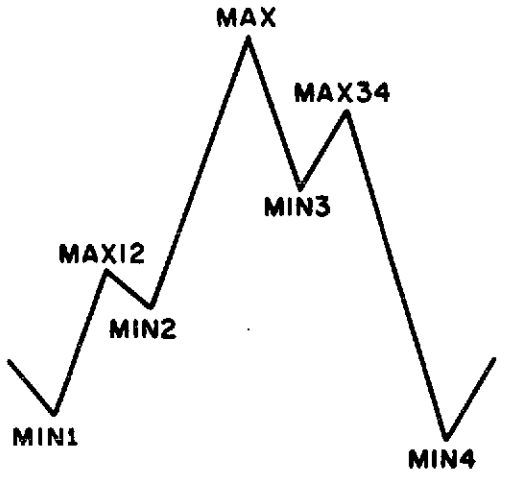

---

13 cm Procedure

5. Test for a smooth direct signal.

IF (2.0·MIN1.GE.MIN2) and (2.0·MIN4.GE.MIN3) ⇒ smooth direct signal.

If the direct signal is smooth then all values between MIN2 and and MIN3 which are greater than CRITC are set equal to CRITC and the procedure is terminated; initial test 1 is then begun on the next frame. If the test for smoothness is failed, then continue with step 6.

6. This procedure is applied only if the direct signal is spread through several frequency analysis bins. Determine the first minimum on either side of the direct signal which

Initial Test (cont.)

satisfies the following condition:

(MIN(I).LT.MIN(I-1)·2.0) Where I indexes the left side of the direct signal

(MIN(J).LT.MIN(J+1)·2.0) and J indexes the right side of the direct signal (see fig. below).

If the conditions are not satisfied in 15 minima, choose the 15th minima. Denote the extreme minima $\hat{I}$, $\hat{J}$. MIN($\hat{I}$) and MIN($\hat{J}$) locate the extent of the spread direct signal. Denote the minima adjacent to the direct signal $\tilde{I}$, $\tilde{J}$. Then replace the data D( ) with D'( ) calculated as follows:

$$D'(L) = D(L) - \frac{D(\tilde{I}) - D(\hat{I})}{\tilde{I} - \hat{I}} \cdot (L-\hat{I}); \quad \hat{I} + 1 \le L \le \tilde{I} - 1$$

$$D'(L) = D(L) - \frac{D(\hat{J}) - D(\tilde{J})}{\hat{J} - \tilde{J}} \cdot (L-\hat{J}); \quad \tilde{J} + 1 \le L \le \hat{J} - 1$$

$$D'(L) = D(\tilde{I}) + \frac{D(\tilde{J}) - D(\tilde{I})}{\tilde{J} - \tilde{I}} \cdot (L-\tilde{I}); \qquad \tilde{I} \le L \le \tilde{J}.$$

7. Terminate procedure; go to next frame, initial test 1.

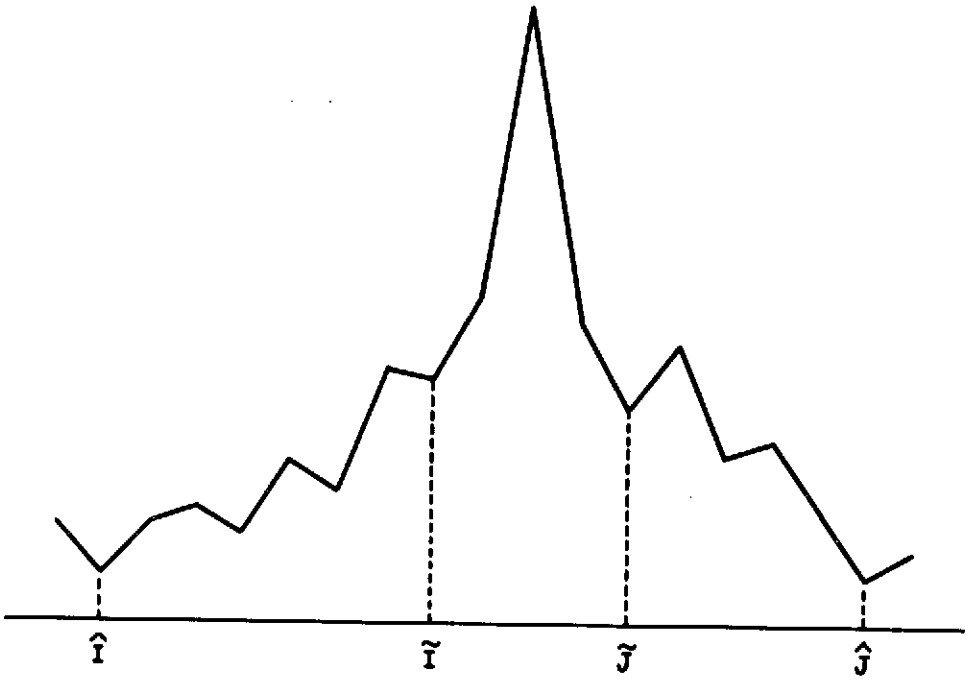

54

116 cm Procedure

8. Find the largest local maximum within 60 Hz of the direct signal on first the left side and then on the right side of the direct signal. Designate these maxima MAXL, MAXR, respectively.

9. Determine relative magnitude of the direct signal.

$$CRITSB = 200.0 \cdot SUM$$

If (MAX.GE.CRITSB) then the direct signal is sufficiently large to require compensation for the sidebands. Replace MAXL and MAXR by the average value of their respective adjacent minima.

10. If (MAX.LT.CRITSB) the direct signal is small. Subtract a constant from the maxima MAXL and MAXR, defined above. The constant is

$$ESUB = (MAX - SUM)/500.0$$

The subtraction is performed only if the data value is greater than ESUB.

11. Replace MAX by the average of MIN2 and MIN3.

12. Terminate procedure and go to next frame, initial test 1.

Appendix VI

Integral Tape Format

The Integral tape contains reduced data records generated in Subtask 7, 8 and 9 (see Block Diagram I). This appendix gives the detailed formatting of that tape and describes all ancillary computations.

A. Tape Organization

The table below gives the file contents and data record length for the Integral tape.

File No.	Contents	Record Length
1	Apollo-14 116 cm	50 words
2	Apollo-14 13 cm	50 words
3	Apollo-15 116 cm	50 words
4	Apollo-15 13 cm	50 words
5	Apollo-16 116 cm	50 words
6	Apollo-16 13 cm	50 words

The tape is 9 track, 800 BPI, binary in XDS Sigma 5 machine images. See Appendix XI for a description of Sigma 5 machine images.

B. File Organization

1. Header Record
2. Data Record

   ⋮

   <many data records>

   ⋮
3. (EOF) End of File
4. Header Record
5. ⋮

56

C. Header Record Format

Word No.	Contents	Units	Machine Type[α]
1-42	Alphanumeric file identifier	--	A
43	Day of year on which data were collected (January 1 = 1)	(days)	I
44	Year data were taken	(year)	I
45-46	Julian Ephemeris Day at 00:00 UT2 on the day the data were taken	(days)	DPR
47-48	Julian Ephemeris Day of reference epoch	(days)	DPR
49	Time increment between center-point of data averaging frame	(sec)	R
50	Number of data records following this header record	--	I

D. Data Record Format (all machine type real)

Word No.		Contents	Units
1		Meaningless	
2		UT2 at midpoint of frame	(sec)
3	X	Components of selenographic unit position vector of spacecraft location	(dim)
4	Y		
5	Z		
6	X	Components of selenographic velocity unit vector	(dim)
7	Y		
8	Z		
9		Speed: Magnitude of spacecraft velocity vector	(m/sec)
10	X	Components of selenographic unit vector from center of the moon to center of the earth	(dim)
11	Y		
12	Z		

[α] A - Alphanumeric
I - Integer
R - Real
DPR - Double Precision Real

D. Data Record Format (all machine type real) (cont.)

Word No.		Contents	Units
13	X	Components of selenographic unit position vector of specular point location	(dim)
14	Y		
15	Z		
16	θ	Euler angles of spacecraft attitude and local horizon frame	(deg)
17	ψ		
18	ϕ		

$$\bar{A}_{veh} = \left[\phi_{(x)}\right]\left[\psi_{(z)}\right]\left[\theta_{(y)}\right]\left[\bar{A}_1\right]$$ (cw rotation looking in + axis direction)

19	α_s	Vehicle look angles to specular point	(deg)
20	β_s		
21	δ	Angle between plane of incidence and plane containing both the vehicle x axis and direction vector to specular point	
22	α_e	Vehicle look angles to earth	(deg)
23	β_e		
24		Selenographic latitude of spacecraft position	(deg)
25		Selenographic longitude of spacecraft position	(deg)
26		Selenographic latitude of specular point	(deg)
27		Selenographic longitude of specular point	(deg)
28		Angle of incidence	(deg)
29		Instantaneous speed of specular point on lunar surface	(m/sec)
30		Predicted bandwidth for rms surface slope of 0.1	(Hz)
31		Reflected doppler minus direct doppler	(Hz)
32		Total doppler shift of reflected signal	(Hz)
33		Component of doppler shift due to earth rotation	(Hz)

D. Data Record Format (all machine type real) (cont.)

Word No.	Contents	Units
34	Altitude of spacecraft above lunar surface: Radius of the moon assumed to be 1736 Km	(Km)
35	Radar cross-section predicted for smooth conducting moon	(dim)
36	(Radar cross-section)/ (received power)	(m^2/w)
37	Polarized power	(arb)
38	Normalized polarized power	(^{o}k)
39	Unpolarized power	(arb)
40	Normalized unpolarized power	(^{o}k)
41	Equivalent area bandwidth	(Hz)
42	Normalized absolute moment bandwidth	(dim)
43	Normalized second moment bandwidth	(dim)
44	Centroid of the echo spectrum	(Hz)
45	RMS slope inferred from equivalent area bandwidth	(deg)
46	Spare if value equals zero, otherwise handscaled one-half power echo bandwidth	(Hz)
47	Data validity flag	
48	Spare if value = 0, otherwise value of spacecraft antenna gain in α_s, β_s, direction (see word no. 19, 20)	(dim)
49	Not used	
50	Data record sequence number	

Note: Data do not always progress uniformly in time. Occasionally, data records will reverse in time for one record, and then continue forward. This effect is caused by the sampling procedure in which a small deliberate overlap was inserted. Time tags on data are correct. Overlapping data correspond to the same time interval but different sampling passes. Slight differences arise from variation in exact times averaged.

E. Data Parameter Definitions

The remainder of this section defines the contents of the data records described just above. The individual subsection numbers correspond to the word numbers in Section D (Data Record Format). If a particular quantity has been described at length elsewhere, a reference will be given. Otherwise, the quantity is defined here.

1. Meaningless

2. Time is the UT2 in seconds at which the data were taken. This time corresponds to the mid-point of the averaging interval, as described under Subtask 4. All trajectory parameters have been interpolated to this time, so that geometrical quantities correspond to the location of the specular point on the mean lunar surface at the middle of the averaging interval.

3, 4, 5. Selenographic Unit Position Vector is defined with respect to the lunar surface. This vector is a unit vector directed from the center of the moon for the instantaneous location of the spacecraft. The X, Y, Z directions are defined as follows:

X = mean earth direction
Y = mean direction of the following limb
Z = north polar direction.

The selenographic coordinates were obtained by rotation from the selenocentric geo-equatorial units of the epoch given in the header record. Procedures are described elsewhere (Tyler, 1968).

6, 7, 8. Selenographic Unit Velocity Vector is a unit vector in the direction of the spacecraft velocity. The coordinate system is the same as that given in items 3, 4, 5 above.

9. Speed is the magnitude of the spacecraft velocity vector.

10, 11, 12. Selenographic Unit Vector to Earth is a unit vector giving the direction from the lunar center of mass to the center of mass to the earth in the selenographic coordinate system described in the 3, 4, 5 above.

13, 14, 15. Selenographic Unit Position Vector of Specular Point is a unit vector from the center of mass of the moon to the location of the specular point on the mean spherical lunar surface. For this computation the lunar radius was taken as 1736 km. The specular point is the location on the mean lunar surface where the angles of incidence and reflection are equal (cf Tyler, 1968).

16, 17, 18. Euler Angles of Spacecraft Attitude connect the spacecraft altitude with a local horizon reference frame. Both the Local Horizon system and the Euler angles are defined in Appendix IX.

19, 20. Look Angles to Specular Point are in vehicle polar coordinates. These quantities are defined in Appendix IX.

21. Plane of the Vehicle , the orientation with respect to the plane of incidence , is given by the angle δ. This quantity is necessary to define the vehicle attitude with respect to the plane of incidence. The angle δ is defined in Appendix IX.

22, 23. Look Angles to Earth are the vehicle polar coordinates of a unit vector in the earth center of mass direction. These quantities were computed in the same manner as items 19, 20 above using the unit vector to earth.

24. Selenographic Latitude of Spacecraft Position is the selengraphic latitude of the subspacecraft point computed from the Z component of the unit vector given in items 3, 4, and 5.

25. Selenographic Longitude of Spacecraft Position is the selenographic longitude of the subspacecraft position computed from items 3, 4, and 5 according to astrometric convention, western limb of the moon leading.

26. Selenographic Latitude of Specular Point is the selenographic latitude of the specular point on a mean spherical lunar surface computed from item 15.

27. Selenographic Longitude of Specular Point is the selenographic longitude of the specular point on the mean spherical lunar surface computed from items 13, 14, 15.

28. Angle of Incidence is the angle of incidence on mean spherical lunar surface at the specular point (cf Tyler, 1968).

29. Speed of the Specular Point is the speed with which the instantaneous specular point moves across the mean lunar surface (Tyler, 1968).

30. Predicted Bandwidth is the one-half power spectral width predicted for an rms surface slope of 0.1, based on the instantaneous angle of incidence and specular point velocity. Computation is after Fjeldbo (1964), also described in Tyler, (1968). Fjeldbo gives a theoretical expression for the 1/2 power echo bandwidth:

$$\Delta f = 4(2\ln 2)^{1/2} \frac{v_s}{\lambda} \frac{h_o}{d_o} \cos\phi \ ,$$

where v_s = velocity of the specular point on the mean lunar surface, λ = wavelength of the radiation (either 116 cm or 13 cm), ϕ = angle of incidence at the specular point, and the quantity $\frac{h_o}{d_o}$ = the mean lunar rms slope.

The quantity Δf is the 1/2 power bandwidth predicted for a gaussian spectrum. Such a spectrum would result from a gently undulating surface with gaussian autocorrelation function.

31. Difference Between Reflected and Direct Doppler Shifts is the predicted frequency difference between a wave reflected from the specular point and the signal traveling directly from the spacecraft to earth. Sign convention is such that the difference is positive for a reflected doppler shift greater than the direct doppler shift.

32. Doppler Shift is the total doppler shift expected from the reflected signal. Computation of this doppler shift included spacecraft motion and the earth's rotation, but did not include the rate of change of distance between the earth and the moon.

33. Doppler Due to Earth's Rotation is the component of the observed doppler shift due to the earth's rotation, for a signal arriving from the direction of the moon.

62

34. Altitude of the spacecraft above the lunar surface has been computed assuming a lunar radius equal to 1736 km. The magnitude of the spacecraft radius vector from the lunar center of mass is obtained by adding the contents of word no. 34 to 1736 km.

35. Normalized Bistatic-Radar Cross-Section is the bistatic-radar cross-section of a smooth conducting sphere of the same radius and relative geometry as the moon. Following Fjeldbo (1964) this cross-section is given by

$$\sigma_B = \frac{4\pi R_1^2 \cos\phi}{\left(\cos\phi + \frac{2d_{or}}{R}\right)\left(1 + \frac{2d_{or}\cos\phi}{R}\right)},$$

where

R_1 = distance from transmitter to the center of the moon

R = lunar radius (1.736×10^6 m)

ϕ = angle of incidence (cf item 28)

d_{or} = distance from the transmitter to the specular point on the mean lunar surface.

36. (Radar Cross Section)/(Received Power) is a multiplicative constant relating instantaneous geometry and received power to surface reflectivity.

$$\frac{\text{radar cross-section}}{\text{received power}} = \frac{(4\pi)^2 R_1^2 R_2^2}{A P_T G_T \sigma_B}$$

where

R_1 = distance from transmitter to center of the moon

R_2 = distance from receiving site to center of the moon

A = effective aperture of receiving antenna

P_T = transmitted power

G_T = transmitting antenna gain in specular point direction

σ_B = bistatic-radar cross-section for a perfectly conducting moon.

For convenience, this expression was evaluated with the following numerical values for the quantities above:

63

R_1 = instantaneous value from MSC trajectory
σ_B = instantaneous value from item 35 above
$R_2 = 4 \times 10^8$ m
$A = 0.5\ (22.5)^2\pi$
$G_T = 1$
$P_T = 2.5$ w.

These values give only order of magnitude results for this experiment.

37. Polarized Power is the experimenter's best estimate of the polarized component of the received echo total power. Extraction of the polarized power is discussed elsewhere (cf Subtask 8).

Denote the polarized power spectrum $P_p(k)$. Consider the figure below. Polarized power is determined from

$$P = \sum_{k=B_1}^{B_2} (P_p(k) - n).$$

The $P_p(k)$ is a polarized power spectrum. In the determination of P, the signal limits B_1, B_2 and n were selected by the experimenter. The quantity n was chosen on the basis of

$$\sum_{B_1'}^{B_2'} (P_p(k) - \hat{n}) \sim 0$$

where B_1', B_2' represent spectral limits containing no echo signal, and $\hat{n}$ represents a sequence of trials of n. The limits B_1, B_2, B_1', B_2', were varied as is necessary to follow the changing echo signal.

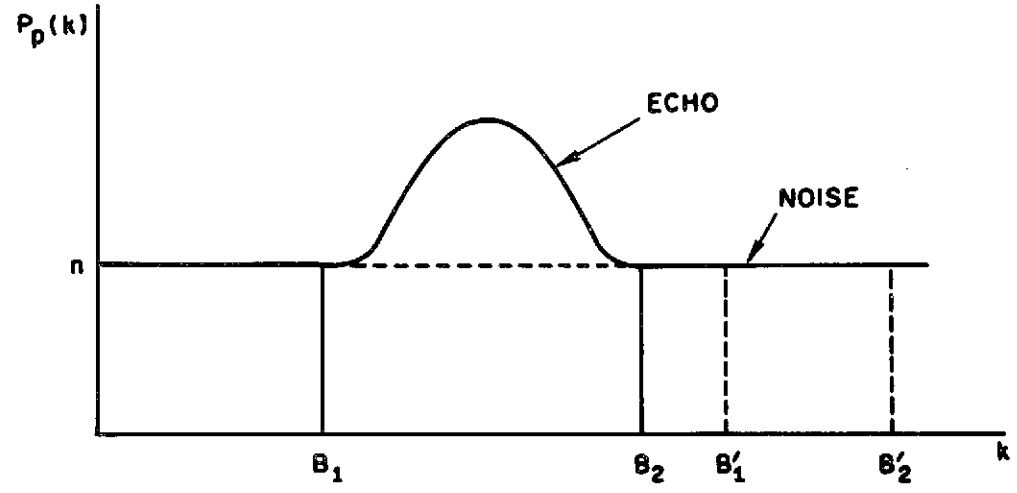

38. Normalized Polarized Power is the quantity contained in item 37 divided by the average power spectral density of the system noise level. This quantity has been discussed in detail elsewhere (cf Subtask 8).

Using the notation introduced under item 37,

$$\text{normalized polarized power} = P/n,$$

where P and n have the same meaning as above.

Note: P/n is extremely sensitive to the choice of n. Thus, polarized power is considered the best overall measure of received polarized echo power. But P/n provides the only method, through the measure of system temperature, of obtaining an absolute power calibration. Similarly, the value of n may be determined from the ratio of polarized power to P/n, so that the variations and system temperature and/or gain may be estimated.

39. Unpolarized Power is the analogous quantity to item 37, for the unpolarized power spectrum. The unpolarized power was obtained in a manner similar to that used to compute polarized power. Letting

$P_u(k)$ represent the unpolarized power spectra, and referring to the figure below, the unpolarized power is given by

$$U = \sum_{\tilde{B}_1}^{\tilde{B}_2} (P_u(k) - \tilde{n}),$$

where the tildas refer to the values of B and n used in the unpolarized power spectrum. In general, the limits for the polarized and unpolarized echoes were different, as was the value of the system noise level. The difference in frequency limits arose from the difference in the spectral distribution of the unpolarized power; the difference in system noise temperature arose from the signal processing used to separate these quantities (cf Subtask 4, 5). The value of $\tilde{n}$ was chosen in a manner similar to that of n in item 37. In some cases, it was not clear that all the unpolarized power is contained in the receiver passband. In this event, $\tilde{B}_1$ or $\tilde{B}_2$ was set equal to the upper or lower frequency limit as appropriate.

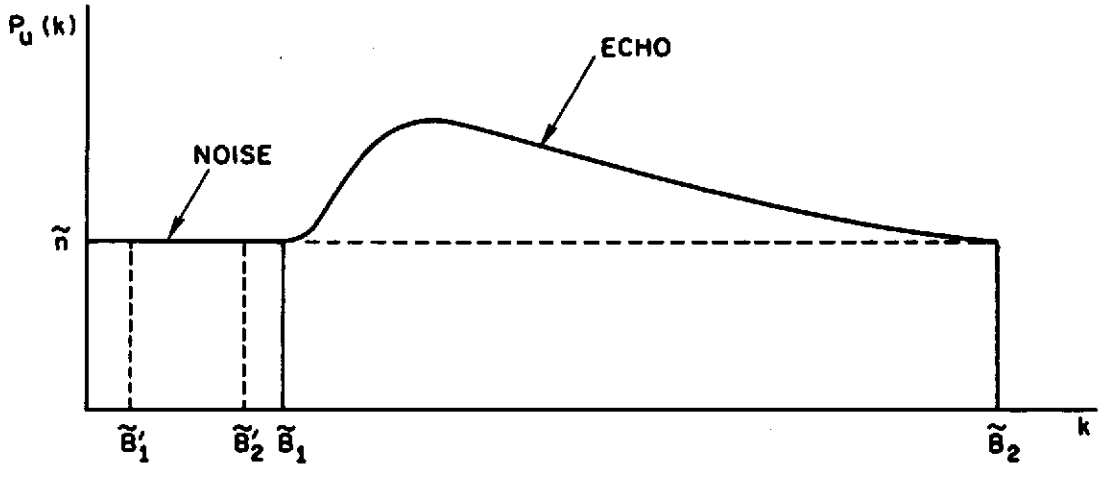

66

40. Normalized Unpolarized Power is the analogous quantity to item 38, for the unpolarized power spectrum. The normalized unpolarized power is defined as

$$\text{normalized unpolarized power} = U/\tilde{n}$$

where the symbols have the same meaning as in item 39. Comments given under item 38 are also germane to normalized unpolarized power.

41.* Equivalent Area Bandwidth: the spectrum of a bistatic-radar echo from a well behaved surface may be written as (Fjeldbo, 1964):

$$S(f) = e^{\frac{-\pi^2 f^2}{2}\left[4v_s(\pi/\lambda)\cos\phi\left(\frac{h_o}{d_o}\right)\right]^{-2}} = e^{-f^2/2\tilde{\sigma}^2},$$

where

f = frequency measured from the centroid of the echo spectrum

v_s = speed of the specular point across the mean lunar surface

λ = wavelength

ϕ = angle of incidence, and

h_o/d_o = unidirectional rms slope.

*The three machine calculated bandwidths, i.e., the equivalent area bandwidth, the absolute moment bandwidth, and the second moment bandwidth, provide three quasi-independent methods of determining the spectral width of the received echoes. The equivalent area bandwidth provides a standard result that is not particularly sensitive to the gaussian, or non-gaussian nature of the echo spectrum. The absolute moment bandwidth and the second moment bandwidth so emphasize departures from gaussian because of the increasing importance given to the wings of the spectrum.

Equivalent area bandwidths have been used to determine lunar rms slopes. The absolute moment bandwidths and the second moment bandwidths, when normalized by the equivalent area bandwidth, give a sensitive measure of the departures of the echo spectra from the gaussian conditions. RMS slopes derived from these measures are termed "gaussian equivalent slopes" in that they would correspond to true surface conditions for a surface with gaussian statistics and a gaussian autocorrelation function with the same equivalent widths. A more complete description of the lunar slopes requires additional analysis (e.g., see Parker and Tyler, 1973).

Solving for rms slope in terms of measured values of standard deviation, $\hat{\sigma}$, of an experimental spectrum yields

$$h_o/d_o = \frac{\hat{\sigma}}{2(v_s/\lambda)\cos\phi} .$$

Thus, the rms slope may be readily determined from an experimental curve in terms of the e^{-1} width of that curve. The equivalent area bandwidth is a measure of $\hat{\sigma}$ based on an equivalent rectangular spectrum of the same area as the experimental spectrum. This width is computed as

$$\hat{\sigma}_{ea} = \frac{\sum_{C_1}^{C_2} P_p(k)}{\max P_p(k)} \cdot (2\pi)^{-1/2}, \quad C_1 < k < C_2.$$

Referring to the figure which follows, the quantity $\hat{\sigma}_{ea} = \sigma$ if the observed curve is gaussian and noiseless. For non-gaussian data $\hat{\sigma}_{ea}$ is still a measure of the bandwidth, although the interpretation must be modified. RMS slopes determined from $\hat{\sigma}_{ea}$ and the expression immediately above will be referred to as equivalent area slopes. The quantity $\hat{\sigma}_{ea}$ is the equivalent area bandwidth.

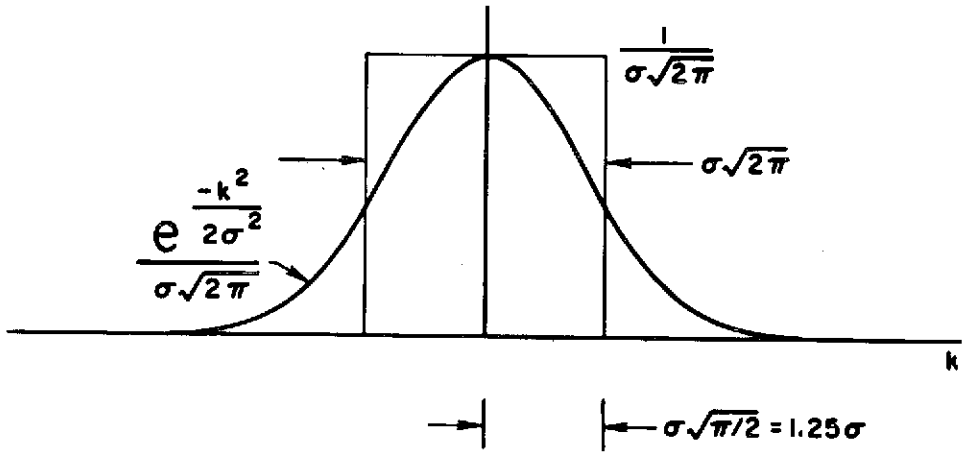

42. Normalized Absolute Moment Bandwidths are based on an equivalent value of $\hat{\sigma}$ computed from the absolute moment of the data. That is,

$$\hat{\sigma}_{am} = \frac{\sum_{k=C_1}^{C_2} P_p(k)\ |k-\bar{k}|}{\sum_{k=C_1}^{C_2} P_p(k)} \cdot \sqrt{\frac{\pi}{2}}\ ; \quad \bar{k} = \frac{\sum_{k=C_1}^{C_2} P_p(k)\ k}{\sum_{k=C_1}^{C_2} P_p(k)}$$

for a gaussian spectrum the equivalent area moments and the absolute moments will be equal

$$\hat{\sigma}_{am} = \hat{\sigma}_{ea} = \sigma$$

where the symbols have the same meaning as in item 41.

The normalized absolute moment bandwidth is

$$\hat{\sigma}_{am}/\hat{\sigma}_{ea}.$$

For a gaussian echo spectrum this ratio will be unity.

43. Normalized Second Moment Bandwidth: the second moment bandwidth is also based on gaussian equivalence. This bandwidth is defined as

$$\hat{\sigma}^2_{sm} = \frac{\sum_{k=C_1}^{C_2} P_p(k)\ (k-\bar{k})^2}{\sum_{k=C_1}^{C_2} P_p(k)}; \quad \bar{k} = \frac{\sum_{k=C_1}^{C_2} P_p(k)\cdot k}{\sum_{k=C_1}^{C_2} P_p(k)}.$$

For a gaussian echo spectrum

$$\hat{\sigma}_{sm} = \hat{\sigma}_{am} = \hat{\sigma}_{ea} = \sigma,$$

where the symbols have the same meaning as under items 42 and 41.

The normalized second moment bandwidth is given by

$$\hat{\sigma}_{sm}/\hat{\sigma}_{ea}.$$

Again, departures of this ratio from unity are indicative of a non-gaussian received echo spectrum

44. Centroid of the Echo Spectrum: the centroid of the echo spectrum is defined in the standard way:

$$\bar{k} = \frac{\sum_{k=C_1}^{C_2} P_p(k)\cdot k}{\sum_{k=C_1}^{C_2} P_p(k)}$$

where the symbols have the same meaning as in 41, 42 and 43. The values of C_1, C_2 are held constant throughout items 41, 42, 43 and 44. The echo spectrum centroid is used in the computations of the absolute moment bandwidths and the second moment bandwidths. It is also useful for estimation of the observed doppler difference (cf item 31). However, the centroid has no direct meaning in an

absolute sense because the transmitter frequencies from the spacecraft are not known precisely.

45. RMS Slopes are obtained from the equivalent area bandwidths according to

$$\frac{h_o}{d_o} = \frac{\hat{\sigma}_{ea}}{2(v_s/\lambda)\cos\phi}$$

and

$$\text{unidirectional rms slope (deg.)} = \tan^{-1}(h_o/d_o),$$

where the results are expressed in degrees for convenience. The quantities v_s, λ, ϕ and $\hat{\sigma}_{ea}$ have been defined in item 41.

46. Handscaled 1/2 Power Echo Bandwidths: handscaling of polarized echo bandwidths has been discussed previously under Subtask 10. A 1/2 power echo bandwidth is defined as the quantity "B" in the figure which follows. In practice, this value was obtained by handscaling data from plots. The handscaled bandwidths provide a rapid, simple technique for the evaluation of lunar rms surface slopes. The handscaled bandwidths were also used as a controlling parameter in development of automated techniques for obtaining echo bandwidths. RMS slopes may be obtained from the handscaled bandwidths by

$$\text{rms slope} = 5.7^{\circ} \times \frac{B}{(\text{predicted 1/2 power bandwidth for rms slope of 0.1})},$$

where the result is given in degrees for convenience. Predicted 1/2 power bandwidths for 0.1 rms slopes are given in word no. 30 of the integral tape data records. Hand measurements were made only for selected segments of the data.

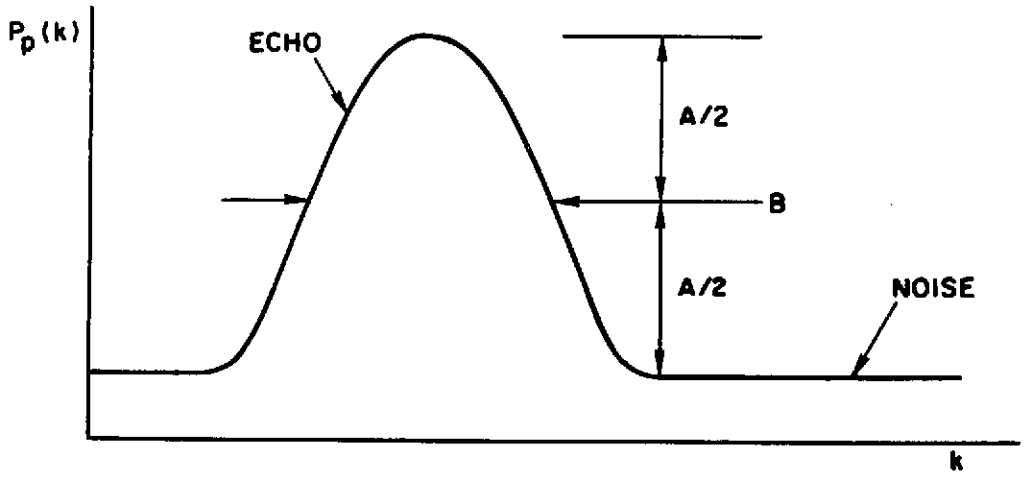

47. Flag: the flag word contains a seven level binary code that indicates data quality. A bit in the "1" condition indicates the existance of a special condition in the data. A bit position in the "0" state carries no meaning other than that the data are normal.

The interpretation of the bit positions is as given below.

Bit in "1" Condition	Implication
1	Polarized power data questionable or no good
2	Unpolarized power data questionable or no good
3	Polarized noise level, n, (cf item 37) changed this data record
4	Polarized integration bounds B_1, B_2, (cf item 37) changed this data record
5	Unpolarized noise level, $\tilde{n}$, (cf item 39) changed this data record
6	Unpolarized integration bounds, $\tilde{B}_1$, $\tilde{B}_2$, (cf item 39) changed this data record
7	System gain changed this data record

Explanation

Bit Position "1"

Polarized data may be flagged for any one of a number of reasons. The presence of interference, an error in setting the integration bounds, or a tape drive error in the data processing are examples of difficulties that would result in such a flag. In case of gross errors the flag represents an objectively known bad data point. In the case of a more subtle phenomenon such as interference, the flag represents an experimenter's subjective opinion. For the 116 cm data interference is the predominant cause of a data bad flags. Data users who wish to examine this question for themselves may do so by reprocessing the data from the JM Doptrack tapes. It is very strongly recommended that no flagged data be used without taking this precaution.

Bit Position "2"

Unpolarized data may be flagged for the same reasons as those given for the polarized data under bit position "1" above. However, because gross errors for polarized and unpolarized data may be independent, and because the unpolarized data possess a certain immunity to interference, which tends to be polarized, the flags in bit position "1" and "2" are not necessarily coincident. As before, in the case of interference, the investigator's judgment is involved.

Bit Position "3"

This flag is set when the noise level, i.e., n in item 37, is changed during the data reduction process. This flag serves to alert the user that such a change has been made. Any discontinuity that occurs when this bit is set is likely to result from this cause. In the case of the polarized power such discontinuities are generally quite small, on the order of 1%. However, in the case of the normalized polarized power such discontinuities may be large, on the order of two. Obviously, no physical significance should be attached to such discontinuities.

Bit Position "4"

Changes in the integration bounds are flagged for reasons similar to those given under bit position "3". The bounds, B_1, B_2, vary with the changing width and location of the polarized echo. Usually, such changes are very small and their effect is not noticable in the data.

Bit Position "5"

Changes in the unpolarized noise level, $\tilde{n}$, are made for the same reasons as those described under bit position "3". As before, changes in the unpolarized power, and especially the normalized unpolarized power, that occur with these changes in $\tilde{n}$ are non-physical.

Bit Position "6"

The comments that apply to the polarized integration bounds given under bit position "4" also apply here.

Bit Position "7"

System gain changes may occur during data reception in the receiving systems or during data playback in the record reproduction system. Such changes are flagged since they will appear as a change in the polarized and unpolarized signal levels. Gain changes do not affect measures of echo bandwidths.

48. Antenna Gain is the gain of the spacecraft antenna in the α_s, β_s direction determined from antenna patterns contained in NAA (1966b) (116 cm), MSC (1967) (Apollo 14, 13 cm), or NAA (1969) (Apollos 15 and 16, 13 cm).

49. Not Used

50. Sequence Number, where the first data record=1.

74

Appendix VII

Cross-Reference Table for JM Doptrack/Integral Tape Trajectory Parameters

The table below provides a cross-reference between the JM Doptrack trajectory parameter records and the Integral tape data records. JM Doptrack tapes are described in Appendix IV. That appendix gives the detailed format for those tapes, but does not define all of the trajectory parameters. Integral tapes are described in detail in Appendix VI. That appendix does include a detailed description of the various trajectory parameters. All of the trajectory parameters given on the JM Doptrack tapes are also found on the Integral tapes. This appendix provides a convenient means for determining the location of a given JM Doptrack tape trajectory parameter in the Integral tape format. For reference, the trajectory parameters are found in the sixth record of a data frame on the JM Doptrack tape (i.e., in record number N·6, N = 1, 2, 3, ..., where the first data record = 1).

JM Doptrack Word No.	is found in	Integral Tape Word No.
1		1
2		2
3		31
4		30
5		28
6		34
7		9
8		35
9		36
10		3
11		4
12		5
13		13
14		14
15		15
16		24
17		25
18		33

Appendix VII (cont.)

JM Doptrack Word No.	is found in	Integral Tape Word No.
19		32
20		26
21		27
22		29
23		22
24		23
25		16
26		17
27		18
28		6
29		7
30		8
31		10
32		11
33		12

Units and scale factors are identical on JM Doptrack and Integral tapes.

Appendix VIII

Matrix Correction Factors

The tables below give the matrix correction factors (c-matrix) that were applied to the 116 cm data in Subtask 5 (cf text). No corrections were applied to the 13 cm data.

In all cases, the following values were used for C_{12} and C_{22}

$$C_{12} = 0.0 + j\ 0.0$$

$$C_{22} = 1.0 + j\ 0.0$$

Only C_{11} and C_{21} were varied. Start times shown below refer to the time on the first frame to which the particular c-matrix was applied; the same c-matrix was used on all succeeding frames with times less than the next entry in the table.

Apollo 14

Time UT2 (sec) start	C-matrix C_{11}	C_{21}
23838.35	1.100 + j 0.0	0.0 + j 0.0
25155.63	1.960 + j 0.0	0.050 + j 0.200
25166.28	1.230 + j 0.0	0.070 + j 0.150
25168.94	1.100 + j 0.0	0.0 + j 0.0
25190.24	1.200 + j 0.0	0.0 + j 0.07
25192.91	1.960 + j 0.0	0.050 + j 0.200
25198.23	1.200 + j 0.0	0.0 + j 0.070
25206.22	1.100 + j 0.0	0.0 + j 0.0
26348.41	0.929 + j 0.0	0.189 + j 0.0

Apollo 15

	C-matrix C_{11}	C_{21}
all data	1.000 + j 0.0	0.0 + j 0.0

Appendix VIII (cont.)

Apollo 16

Time UT2 (sec) start	C-matrix C_{11}	C_{21}
4592.35	0.913 + j 0.0	-0.134 - j 0.045
4780.77	0.958 + j 0.0	-0.040 - j 0.010
5432.35$^{\alpha}$	0.944 + j 0.0	-0.055 - j 0.032
5587.79	1.000 + j 0.0	-0.060 + j 0.020
5983.46	0.900 + j 0.0	-0.100 - j 0.050
6272.35$^{\alpha}$	0.830 + j 0.0	-0.100 - j 0.040
6484.32	0.870 + j 0.0	-0.090 + j 0.0
7030.72	0.860 + j 0.0	-0.060 - j 0.050
7112.35$^{\alpha}$	0.871 + j 0.0	-0.072 - j 0.490
7333.74	0.815 + j 0.0	-0.066 + j 0.010
7701.15	0.778 + j 0.0	-0.060 - j 0.040
7952.35$^{\alpha}$	0.740 + j 0.0	-0.100 - j 0.040

$^{\alpha}$These changes are located in overlap areas described in Appendix IV (D3). The change takes effect on the frame with the time (word 2, record 6; cf Appendix IV) closest to that shown here.

78

Appendix IX

Coordinate Transformations

A. General Definitions

$\bar{r}$ = specular point position vector

$\bar{p}$ = spacecraft position vector

$\bar{v}$ = spacecraft velocity vector

$\bar{a}_{\Delta H}$ = vector in local horizon system

$\bar{a}_{\Delta V}$ = vector in vehicle reference frame

$\bar{a}_{\Delta P}$ = vector in primary or principal reference system

$\left.\begin{matrix}\emptyset \\ \Psi \\ \theta\end{matrix}\right\}$ defined in C below (Euler angles between local horizon and vehicle systems)

$\left.\begin{matrix}\alpha \\ \beta\end{matrix}\right\}$ look angles to specular point in vehicle system

$\delta\}$ orientation of vehicle along α, β direction (defined below)

B. Data supplied by MSC gives spacecraft attitude in "Local Horizontal" coordinate system.

Definition of "Local Horizontal" system (see figure which follows):

$$\bar{a}_{ZH} = -\frac{\bar{p}}{/\bar{p}/}$$

$$\bar{a}_{YH} = \frac{\bar{v} \times \bar{p}}{/\bar{v} \times \bar{p}/}$$

$$\bar{a}_{XH} = \bar{a}_{YH} \times \bar{a}_{ZH}.$$

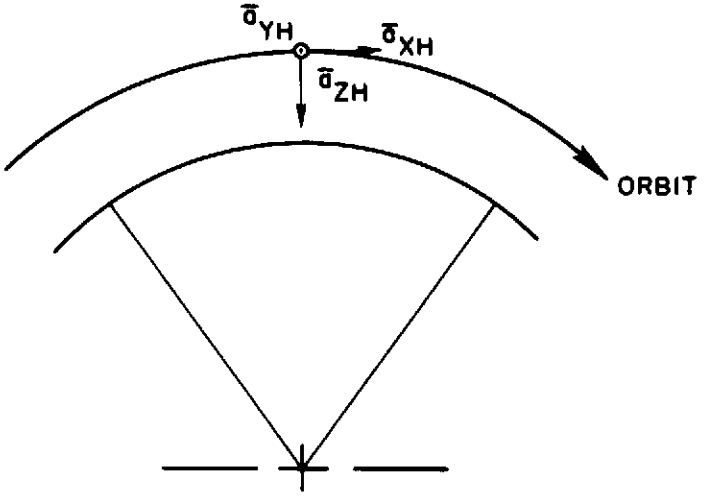

$\bar{a}_{ZH}$ is directed toward the nadir.

$\bar{a}_{YH}$ is directed along angular momentum vector.

$\bar{a}_{XH}$ is in the plane of the orbit roughly along $\bar{v}$.

C. Specification of spacecraft attitude

The Euler angles $\emptyset$, Ψ, θ specify the sequence of rotations required to transform Local Horizontal coordinates to Vehicle coordinates as follows:

$$\begin{bmatrix} X_V \\ Y_V \\ Z_V \end{bmatrix} = \begin{bmatrix} \emptyset \\ (X) \end{bmatrix} \begin{bmatrix} \Psi \\ (Z) \end{bmatrix} \begin{bmatrix} \theta \\ (Y) \end{bmatrix} \begin{bmatrix} X_H \\ Y_H \\ Z_H \end{bmatrix}$$

where the matrix $\begin{bmatrix} (\text{ang}) \\ (\text{axis}) \end{bmatrix}$ denotes a rotation of (ang) about the current (axis). Rotations are in the sequence (Y, Z, X). The sense of rotation is clockwise when looking in the + (axis) direction. For instance, consider:

$$\begin{bmatrix} X_1' \\ X_2' \\ X_3' \end{bmatrix} = \begin{bmatrix} \alpha \\ (X_1) \end{bmatrix} \begin{bmatrix} X_1 \\ X_2 \\ X_3 \end{bmatrix}$$

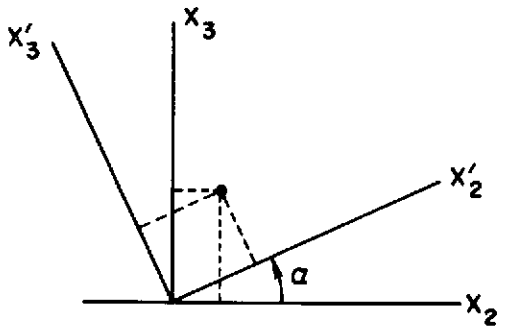

$$X_1' = X_1$$

$$X_2' = X_2 \cos\alpha + X_3 \sin\alpha$$

$$X_3' = -X_2 \sin\alpha + X_3 \cos\alpha$$

then the transformation is

$$\begin{bmatrix} X_1' \\ X_2' \\ X_3' \end{bmatrix} = \begin{bmatrix} 1 & 0 & 0 \\ 0 & \cos\alpha & \sin\alpha \\ 0 & -\sin\alpha & \cos\alpha \end{bmatrix} \begin{bmatrix} X_1 \\ X_2 \\ X_3 \end{bmatrix}$$

Thus

$$\begin{bmatrix} \phi \\ (X) \end{bmatrix} \begin{bmatrix} \Psi \\ (Z) \end{bmatrix} \begin{bmatrix} \theta \\ (Y) \end{bmatrix} = \begin{bmatrix} R \end{bmatrix}$$

$$\begin{bmatrix} R \end{bmatrix} = \begin{bmatrix} \cos\Psi\cos\theta & \sin\Psi & -\cos\Psi\sin\theta \\ \sin\phi\ \sin\theta - \cos\phi\sin\Psi\cos\theta & \cos\phi\cos\Psi & \cos\phi\sin\Psi\sin\theta + \sin\phi\cos\theta \\ \sin\phi\sin\Psi\cos\theta + \cos\phi\sin\theta & -\sin\phi\cos\Psi & \cos\phi\cos\theta - \sin\phi\sin\Psi\sin\theta \end{bmatrix}$$

D. Conversion of Reference Coordinate to Local Horizontal System

Quantities that are known in the principal reference system may be converted to the Local Horizon system through the directional cosines connecting the two. These are given by the vector components of the $\bar{a}_{\triangle H}$, expressed in the primary system. The $\bar{a}_{\triangle H}$ form the rows of the

81

transformation (rotation only) matrix. Thus

$$\begin{bmatrix} \bar{X}_H \end{bmatrix} = \begin{bmatrix} a_{XH_1} & a_{XH_2} & a_{XH_3} \\ a_{YH_1} & a_{YH_2} & a_{YH_3} \\ a_{ZH_1} & a_{ZH_2} & a_{ZH_3} \end{bmatrix} \begin{bmatrix} \bar{X}_P \end{bmatrix}$$

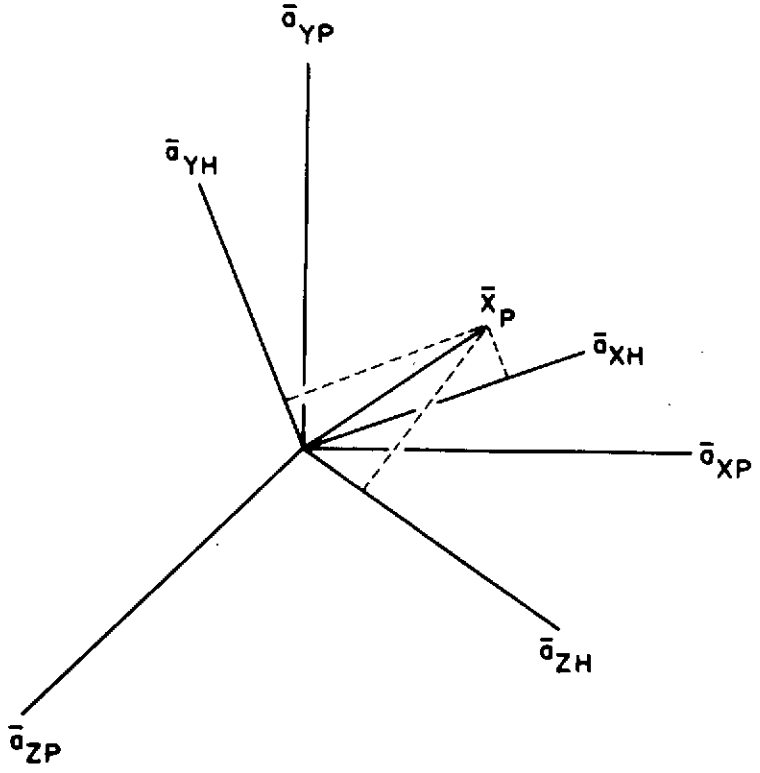

Components in sub -H system are projections onto reference axes of that system.

82

E. Conversion of Reference Coordinates for Vehicle Coordinates

Conversion from principal coordinates to Vehicle coordinates may be made by two successive rotations, principal coordinates $\longrightarrow$ Local Horizontal coordinates Local Horizontal coordinates $\longrightarrow$ Vehicle coordinates.

or

$$\left[\bar{X}_V\right] = \left[R_{VH}\right]\left[X_H\right] = \left[R_{VH}\right]\left[R_{HP}\right]\left[\bar{X}_P\right]$$

where R_{ij} implies a rotation from the j to i system. Thus $\left[R_{VP}\right] = \left[R_{VH}\right]\left[R_{HP}\right]$.

F. Computation of spacecraft to specular point look angles, α_s, β_s.

1. The direction to the specular point from the spacecraft is

$$\frac{\bar{r} - \bar{p}}{|\bar{r} - \bar{p}|} = \bar{\gamma}.$$

In Vehicle coordinates

$$\left[\bar{\gamma}_V\right] = \left[R_{VP}\right]\left[\bar{\gamma}_P\right].$$

The quantity α is measured from the + X direction,

$$\therefore \alpha_s = \arccos(\gamma_{XV}), \quad 0 \leq \alpha \leq \pi.$$

The quantity β_s is the azimuthal angle (minimum angle to $\bar{\gamma}$, X_V plane) measured from the $-Z_V$ axis, positive towards $+ Y_V$:

$$\beta_s = \text{signum}\,(\gamma_{YV}) \cdot \arccos(-\gamma_{ZV}), \quad -\pi \leq \beta \leq \pi,$$

where $\text{signum}(X) = \frac{X}{|\bar{X}|}$. These quantities are depicted in the figure which follows:

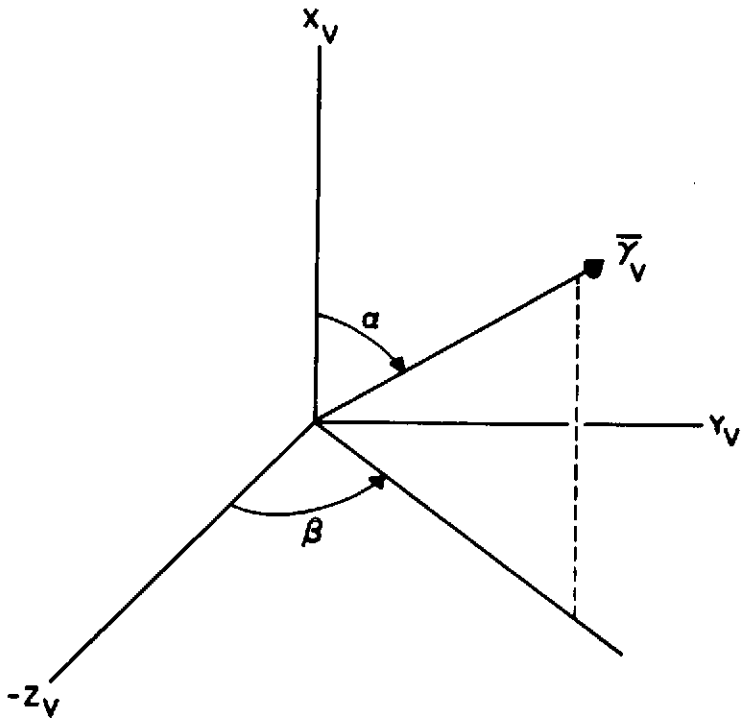

G. Definition and Computation of δ.

The angle δ is the included angle between the $\bar{\gamma}$, $\bar{a}_{XV}$ plane and the plane of incidence, the $\bar{\gamma}$, $\bar{p}$ plane (see figure which follows):

$$\delta = \text{signum}\left(\bar{p} \cdot \bar{a}_{XV} \otimes \bar{\gamma}\right) \cdot \arccos\left(\frac{\bar{\gamma} \otimes \bar{p}}{\bar{\gamma} \otimes \bar{p}} \cdot \frac{\bar{a}_{XV} \otimes \bar{\gamma}}{\bar{a}_{XV} \otimes \bar{\gamma}}\right),$$

$$-\pi \leq \delta \leq \pi.$$

84

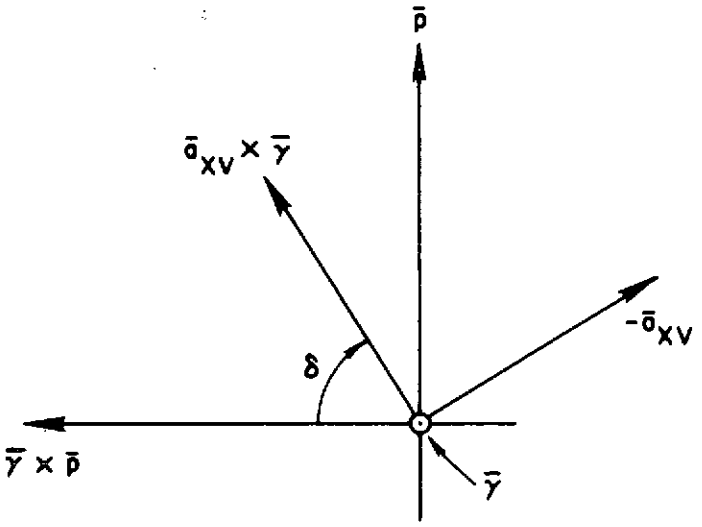

H. Sources

Additional information regarding the definitions of Local Horizon and Vehicle coordinates may be found in MSC publications describing trajectory tapes (MSC, 1970). Input for α_s, β_s, δ computations are MSC supplied experimenter trajectory tapes. The principle reference frame is selenographic.

Appendix X

Relationship Between the Coherency Matrix and Other Specifications of Polarization

The methods used to estimate the polarization state of Apollo bistatic-radar data are those described by Tyler and Simpson,(1970). This appendix describes the relationship of the coherency matrix to the more common descriptors intensity, axial ratio and orientation of the polarization ellipse.

The coherency matrix is from Born and Wolf, (1959).

$$\bar{e}_1(t) = \mathrm{Re}\left\{ E_1 \, e^{j\omega t} \right\} \bar{e}_1$$

$$\bar{e}_2(t) = \mathrm{Re}\left\{ E_2 \, e^{j\omega t} \right\} \bar{e}_2$$

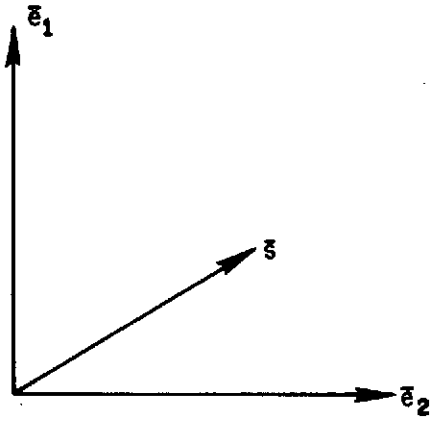

$$\underline{J} = \begin{bmatrix} \langle E_1 E_1^* \rangle & \langle E_1 E_2^* \rangle \\ \langle E_1^* E_2 \rangle & \langle E_2 E_2^* \rangle \end{bmatrix}$$

where E_1, E_2 are complex magnitudes associated with any pair of orthogonal linear polarizations.

$$\underline{J} = \begin{bmatrix} J_{11} & J_{12} \\ J_{21} & J_{22} \end{bmatrix}; \quad J_{ij} = \langle E_i E_j^* \rangle$$

86

$$\underline{\rho} = \mathrm{Tr}(\underline{J}) \begin{bmatrix} \rho_{11} & \rho_{12} \\ \rho_{21} & \rho_{22} \end{bmatrix} \; ; \; \mathrm{Tr}(J) = J_{11} + J_{22} = \text{total received power}$$

Born and Wolf show that the percentage polarization γ, i.e., the fraction of $\mathrm{Tr}(\underline{J})$ that may be described by a deterministic polarization ellipse, is

$$\gamma = \sqrt{1 - 4\,(\rho_{11}\,\rho_{22} - \rho_{12}\,\rho_{21})}.$$

Then any $\underline{J}$ may be written as

$$\underline{J} = \underbrace{\frac{1}{2}\,(1-\gamma)\,\mathrm{Tr}(\underline{J}) \begin{bmatrix} 1 & 0 \\ 0 & 1 \end{bmatrix}}_{\text{unpolarized part}} + \underbrace{\gamma\,\mathrm{Tr}(\underline{J}) \begin{bmatrix} q_{11} & q_{12} \\ q_{21} & q_{22} \end{bmatrix}}_{\text{polarized part}}$$

where

$$q_{ii} = \frac{1}{\gamma}\,\left(\rho_{ii} - \frac{1}{2}\,(1-\gamma)\right) \; ; \; q_{ij} = \frac{1}{\gamma}\,\rho_{ij}.$$

Ko (1962) gives the relationship between $\underline{q}$ and the Poincaré sphere (Beckmann, 1968) as: (shown schematically in the figure which follows)

$$q_{11} = \cos 2\omega, \qquad 0 \le \omega \le \pi$$

$$q_{12} = \sin\omega\,\cos\omega\,e^{j2\chi} \Rightarrow \tan 2\chi = \frac{\mathrm{Im}(q_{12})}{\mathrm{Re}(q_{12})}\,, \; -\frac{\pi}{2} < 2\chi < \frac{\pi}{2}.$$

Also note:

$$\tan\omega = \sqrt{\frac{q_{22}}{q_{11}}}, \; \tan\chi = \frac{M}{N}\,, \quad \tan\chi > 0 \Rightarrow \text{right elliptical polarization.}$$

87

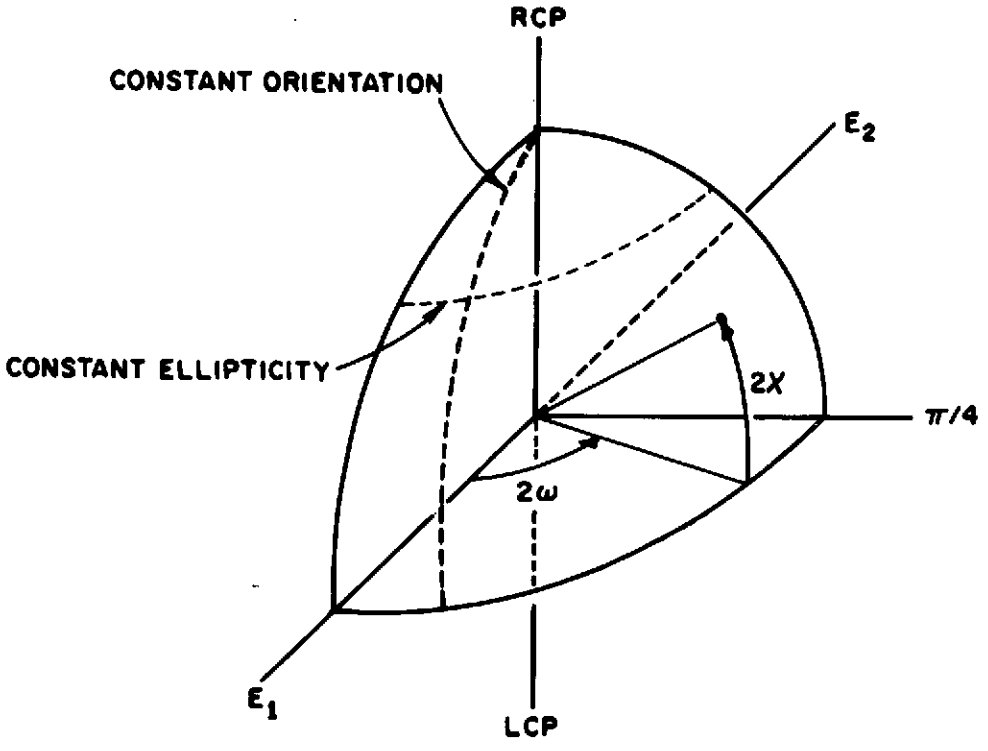

For Apollo, a similar matrix $\underline{J}_c$, where the sub-c designates decomposition of the incident wave into circular components, is used:

$$\underline{J}_c = \begin{bmatrix} \langle E_\ell E_\ell^* \rangle & \langle E_\ell E_r^* \rangle \\ \langle E_\ell^* E_r \rangle & \langle E_r E_r^* \rangle \end{bmatrix} \qquad \begin{bmatrix} J_{c11} & J_{c12} \\ J_{c21} & J_{c22} \end{bmatrix}$$

where E_ℓ and E_r denote left and right circular waves.

Defining $\underline{\rho}_c$ and $\underline{q}_c$ in an analogous manner:

$$\underline{J}_c = \begin{bmatrix} \rho_{c11} & \rho_{c12} \\ \rho_{c21} & \rho_{c22} \end{bmatrix} = \frac{1}{2}(1-\gamma)\,\mathrm{Tr}(\underline{J}_c) \begin{bmatrix} 1 & 0 \\ 0 & 1 \end{bmatrix} + \gamma\,\mathrm{Tr}(\underline{J}_c) \begin{bmatrix} q_{c11} & q_{c12} \\ q_{c21} & q_{c22} \end{bmatrix}, \text{ where}$$

as before $\gamma = \sqrt{1 - 4\,(\rho_{c11}\,\rho_{c22} - \rho_{c12}\,\rho_{c21})}$.

However, the interpretation of the $\underline{q}_c$ is modified in accordance with the new definition:

$$\tan\chi = \frac{M}{N} = \frac{-\sqrt{q_{c11}} + \sqrt{q_{c22}}}{\sqrt{q_{c11}} + \sqrt{q_{c22}}}$$

$$\omega = \frac{1}{2}\arg(q_{12}),$$

where ω is referenced to instantaneous E_ℓ position at time $t = 0$.

The invariance of $\mathrm{Tr}(\cdot)$, $\mathrm{Det}(\cdot)$, and γ under transformations to circular coordinates can be verified by direct computation.

89

Appendix XI

XDS Sigma 5 Machine Images

All data on the JM Doptrack and Integral tapes are in the form of XDS Sigma 5 machine images. One word is 32 bits, one byte, 8 bits. The data are either real (floating-point), integer, or alphanumeric. The machine images are as follows:

A. Real

A single precision real number consists of a sign bit (bit 0), a biased[α], base 16 exponent called a characteristic (bits 1-7), and a 24 bit fraction. A double precision number consists of a single precision number followed by an additional 32 bits of fractional significance (cf figure below). Unless otherwise noted, all numbers referred to in this report as "real" are single precision.

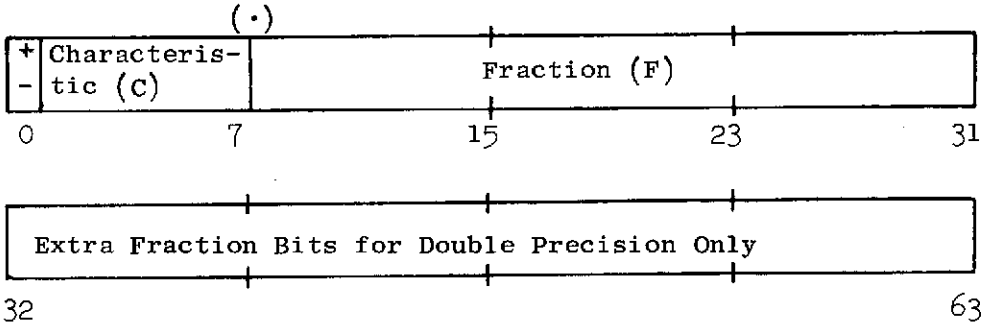

[α]The bias value of 64_{10} is added to the exponent to make it possible to compare the absolute magnitude of two numbers without reference to a sign bit.

A real number (N) is defined as follows:

$N = F \times 16^{C-64}$ where

$F = 0$ or

$2^{-24} \leq |F| < 1$ (single precision) or

$2^{-56} \leq |F| < 1$ (double precision)

and $0 \leq C \leq 127$

A negative real number is the two's complement of its positive representation. (Note that this differs from the IBM 360.)

B. Integer

Integers are written in full-word, two's complement representation.

C. Alphanumeric

Alphanumeric data, strings of characters, are represented in Extended Binary-Coded-Decimal Interchange Code (EBCDIC). Each character occupies one byte (8 bits), so each word of alphanumeric data contains four characters.

References

Beckmann, P., The Depolarization of Electromagnetic Waves, The Golem Press, Boulder, Colorado, 1968.

Blackman, R. B. and J. W. Tukey, The Measurement of Power Spectra, Dover Publications, Inc., New York, 1958.

Born, M. and E. Wolf, Principles of Optics, Pergamon Press, New York 1959.

Howard, H. T. and G. L. Tyler, "Bistatic-Radar Studies of the Lunar Surface," Apollo 14 Preliminary Science Report, NASA publication SP-272, 1971.

Howard, H. T. and G. L. Tyler, "Bistatic-Radar Investigation," Apollo 15 Preliminary Science Report, NASA publication SP-289, p. 23-1, 1972.

Howard, H. T. and G. L. Tyler, Apollo 16 Preliminary Science Report, NASA publication SP-315, p. 25-1, November, 1972.

Ko, H. C., Proc. IRE, pp. 1950-1956, September, 1962.

Tyler, G. L. and H. T. Howard, "Bistatic-Radar Observations of the Lunar Surface with Apollos 14 and 15," paper presented at Third Lunar Conference, Houston, Texas, January, 1972.

Tyler, G. L. and D. H. H. Ingalls, "Functional Dependence of Bistatic Radar Frequency Spectra on Lunar Scattering Laws," J. Geophys. Res., Vol. 76, No. 20, pp. 4775-4785, July, 1971.

Tyler, G. L. and R. A. Simpson, Bistatic-Radar Studies of the Moon with Explorer 35, Final Report: Part 2, Scientific Report No. 3610-2, Stanford Electronics Laboratories, October, 1970.

Tyler, G. L., Estimation of Polarization with Arbitrary Antennas, Scientific Report No. 3610-1, SU-SEL-70-064, Stanford Electronics Laboratories, October, 1970.

DSN, 1970, Operations Plan for Apollo 14, Vol. VI, Report No. 609-37, Jet Propulsion Lab., Pasadena, California, 15 December 1970.

DSN, 1971, Operations Plan for Apollo 15, Vol. VII, Report No. 609-38, Jet Propulsion Lab., Pasadena, California, 1 January 1971.

DSN, 1972, DSN/Flight Project Interface Design Handbook, Deep Space Network Standard Practice Doc. No. 810-5C, Jet Propulsion Lab., Pasadena, California, 1 April 1972.

MSC, 1967, Full Scale Block II Command and Service Module S-Band Omni Antenna Patterns, MSC Report No. 67-EE-15, Project Apollo, Manned Spaceflight Center, Houston, Texas, June, 1967.

92

MSC, 1970, "Apollo Postflight Trajectory Parameters," MSC Internal Note No. 70-FM-21 (MSC-01564), Manned Spaceflight Center, Houston, Texas, 13 February 1970.

MSC, 1970, Bistatic Test Data Package (VHF Spectrum and LM S-Band Interference)," MSC Report No. MSC-EE7-70-115(u), Manned Spaceflight Center, Houston, Texas, 18 December 1970.

NAA, 1966a, Radiation Distribution Plots of Linear Polarization Data Types, Report No. NAA 66H-343, North American Aviation, Columbus, 20 April 1966.

NAA, 1966b, VHF SM/SLA Scimitar Antenna, FDWA M 6547, Second Pattern Report, 2 Vols., Report No. NA 66H-81, North American Aviation, Columbus, 1966 (no further data given).

NAA, 1969, High-Gain Antenna Equipment Characteristics and Operation 106 and Subsequent S/C, Report No. TDR 69-042, Revision 1, North American Rockwell Space Division, Downey, April, 1969.

93

NOTES

Block Diagram I: Block Diagram of

Stanford Apollo Bistatic-Radar Data Processing and Reduction

(1) a) Receiving system described in Appendix I.

b) Critical filter response given in Appendix III.

c) RCP, LCP, coherency maintained through entire system.

d) Antenna pointing maintained toward center of moon using Stanford Research Institute lunar ephemeris.

e) Absolute phase in LCP, RCP channels not controlled, relative phase maintained.

f) Spectral purity of downlink signals measured for Apollo equipment type (MSC, 1970).

(2) a) Deep space network station under NASA control, used standardized procedures except as noted.

b) Apollo operational system used for 64 m dish pointing, closed loop receiver acquisition. Station configuration for bistatic-radar experiment described elsewhere (DSN, 1970, 1971).

c) Absolute phase in RCP, LCP not controlled, relative phase maintained.

(3) a) Stanford Signal Conditioning Unit provided critical control over system frequency response. Filter characteristics given in Appendix III.

b) FR1400 tape recorders A, B used to provide continuous data across tape changes.

(4) a) H.P. 3955B frequency response adjusted for a maximally flat frequency response on playback using calibration tapes from data source machine (H.P. 3955B for 116 cm data; FR1400 A, B for 13 cm data).

b) Coherent sampling maintained. Reference signal from tape used to synchronize samples.

c) Actual time recovered by use of time code translator clock output to establish start times. Time from start maintained by counting sampling pulses.

94

C-2

(4) d) Actual sampling rates: (cont.)

Flight	Wavelength	Sampling Rate	Ratio of Effective Sampling Rate to Actual Sampling Rate
Apollo 14	13 cm	10.75 kHz	4
Apollo 14	116 cm	10.00 kHz	1
Apollo 15	13 cm	10.75 kHz	4
Apollo 15	116 cm	10.00 kHz	1
Apollo 16	13 cm	21.5 kHz	2
Apollo 16	116 cm	10.00 kHz	1

(5) a) Fourier coefficients computed from successive groups of weighted data: data group length either 1024 or 2048 samples, weighting function is $\sin^2 (\pi t/T)^T$, where t is time and T is duration of sample group length.

b) Data analysis lengths

Data Source	Sample Length	Analysis bandwidth (Hz)
Apollo 14 S-band	1024	42.0
Apollo 14 VHF	1024	9.8
Apollo 15 S-band	1024	42.0
Apollo 15 VHF	2048	4.9
Apollo 16 S-band	1024	42.0
Apollo 16 VHF	2048	4.9

(6) Polarimeter computed elements of signal covariance matrix (see Subtask 5).

(7) a) Normalizing data obtained from data runs employing noise input. Purpose was to compensate for variations in receiver passband.

b) Normalizing tapes contain smoothed power spectra from noise source data.

(8) a) C-matrix correction was polarization coordinate transformation to correct for errors in receiver antenna system. Applied to 116 cm data only.

b) Criterion for choosing c-matrix was to minimize polarized part of system noise.

95

(9) a) Merge combined data tapes with geometrical parameters obtained from MSC (Best-Estimate-Trajectory) Post-Flight tapes.

b) MSC data are interpolated to center of data averaging window.

c) JM Doptrack tapes constitute primary data source for analysis.

(10) Carrier suppression deleted direct signal from the data by means of an empirical algorithm (see Subtask 7 and Appendix V).

(11) a) Tapes edited for changes indicated in operational logs and interference.

b) Handscaled data added to tape from card source.

c) Edited integral tapes constitute reduced data records.

Page intentionally left blank